



Jakob Lidl, BSc

# **Accuracy Investigation of the AIBotix X6 V2 Unmanned Aerial System employing relative GNSS measurements for direct georeferencing**

## **Master's Thesis**

to achieve the university degree of  
Master of Science

Master's degree programme: Geomatics Science

submitted to

**Graz University of Technology**

Supervisor

Univ.-Prof. Dipl.-Ing. Dr.techn. Werner Lienhart

Institute of Engineering Geodesy and Measurement Systems

Head: Univ.-Prof. Dipl.-Ing. Dr.techn. Werner Lienhart

Graz, January 2017

## Affidavit

I declare that I have authored this thesis independently, that I have not used other than the declared sources/resources, and that I have explicitly indicated all material which has been quoted either literally or by content from the sources used. The text document uploaded to TUGRAZonline is identical to the present master's thesis.

---

Date

---

Jakob Lidl

# Acknowledgement

I want to thank Univ.-Prof. Dipl-Ing. Dr.techn. Werner Lienhart for his advice and council during this thesis. The technical discussions with him always helped me make progress in this thesis and provided me with ideas on how to conduct the experiments as well as the processing.

Univ.-Prof. B.A. M.Sc. Ph.D. Scott Kieffer I want to thank for bringing this topic to our attention, and for providing the UAS as well as granting me access to the computers and software of the Institute of Applied Geosciences.

Maja Bitenc, MSc helped me with my experiments and explained the functionality of the drone, as well as the respective software to me. She also communicated most upcoming problems to the manufacturer of the drone, and gave input on how to approach them.

Gerhard Lauk and Mag. Peter Schreiber from the Institute of Applied Geosciences, and Ing. Rudolf Lummerstorfer from the Institute of Engineering Geodesy and Measurement Systems deserve thanks for helping me with numerous experiments.

My colleges and friends Peter Bauer and Fabian Buchmayer I too want to thank for helping me with my experiments, but also for the interesting discussions and inputs during the coffee breaks in the office.

I want to thank Claudia Gafko for her support and her love, not only during this thesis but also for the last 5 years.

Finally, I want to thank my parents Christian and Sonja and also my sister Alina. They supported me during my education and enabled me a wonderful childhood free of sorrows.

Thank you all!

# Abstract

In this thesis, the accuracy of a novel approach for georeferencing of aerial photos taken from a UAS is assessed, to find possible applications in the geodetic-, as well as in the geological field. The AIBotix X6 V2 Unmanned Aerial System (UAS) is equipped with a Novatel GNSS unit containing a geodetic GNSS receiver and antenna. This allows for precise relative GNSS measurements which result in GNSS solutions with centimetre accuracy. The camera position is calculated from this solution and can be used instead of Ground Control Points (GCPs) for georeferencing the pictures. This novel approach considerably minimises the time required in the field and also does not require access to the measurement area. The photogrammetric measurements using the novel approach are verified by terrestrial measurements taken by a Robotic Total Station (Leica MS60), as well as photogrammetric measurements using the conventional approach, i.e. employing GCPs. Using the novel approach, the camera positions could be determined with an accuracy of 2.2 cm, leading to a ground point accuracy of 5.8 cm. For geological applications, the determination of rock face orientations was simulated by calculating the orientation of rooftops from the point cloud. The mean absolute difference between the orientations calculated in the conventional and the novel way was 0.14 degrees, which falls way below the required accuracy of one degree for the respective application.

# Zusammenfassung

In dieser Masterarbeit wird die Genauigkeit eines neuen Ansatzes zur Georeferenzierung von Fotos, die von einer Drohne aus aufgenommen werden untersucht, um mögliche Anwendungen für den geodätischen- und für den geologischen Bereich zu finden. Die "AIBotix X6 V2" Drohne ist mit einer Novatel GNSS Einheit ausgestattet, die eine geodätischen GNSS Antenne und einen entsprechenden Empfänger enthält. Dadurch ist es möglich, präzise relative GNSS Messungen durchzuführen und GNSS Positionslösungen mit Zentimeter Genauigkeit zu erhalten. Aus diesen Lösungen werden die Positionen der Kamera berechnet, die anstatt von Ground Control Points (GCPs) für die Georeferenzierung der Fotos verwendet werden können. Dieser Ansatz minimiert die erforderliche Zeit im Feld erheblich und benötigt weiters keinen direkten Zugang zum Projektgebiet. Die photogrammetrischen Messungen unter Verwendung des neuen Ansatzes werden mittels terrestrischer Messungen einer motorisierten Totalstation (Leica MS60) und photogrammetrischer Messungen unter Verwendung des herkömmlichen Ansatzes (Einsatz von GCPs) verifiziert. Die Kamerapositionen konnten unter Verwendung des neuen Ansatzes mit einer Genauigkeit von 2.2 cm bestimmt werden, was zu einer Genauigkeit von 5.8 cm für Bodenpunkte führte. Für geologische Anwendungen wurde die Orientierungsbestimmung von Felsflächen simuliert, indem die Orientierung von Hausdächern aus der Punktwolke berechnet wurde. Die mittlere absolute Differenz zwischen den Orientierungen des neuen und des herkömmlichen Ansatzes betrug 0.14 Grad, was die erforderliche Genauigkeit von einem Grad bei weitem unterschreitet.

# Abbreviations

<b>AGRP</b>	Actual General Reference Point
<b>APOS</b>	Austrian Positioning Service
<b>ASCII</b>	American Standard Code for Information Interchange
<b>C2C</b>	Cloud-to-Cloud comparison
<b>C2M</b>	Cloud-to-Mesh comparison
<b>CCF</b>	Cross Correlation Function
<b>DGPS</b>	Differential GPS
<b>DPC</b>	Dense Point Cloud
<b>EPOSA</b>	Echtzeit Positionierung Österreich
<b>GCP</b>	Ground Control Point
<b>GGRP</b>	Given General Reference Point
<b>GNSS</b>	Global Navigation Satellite System
<b>GPS</b>	Global Positioning System
<b>GLONASS</b>	Globalnaja nawigazionnaja sputnikowaja sistema
<b>IMU</b>	Inertial Measurement Unit
<b>M2M</b>	Mesh-to-Mesh comparison
<b>M3C2</b>	Multiscale-Model-to-Model-Cloud comparison
<b>MPE</b>	Mean Point Error
<b>OTF</b>	On The Fly
<b>PET</b>	Precise Event Timestamp
<b>POI</b>	Point Of Interest
<b>PP</b>	Post Processing
<b>PS</b>	Agisoft PhotoScan
<b>RINEX</b>	Receiver Independent Exchange Format
<b>RTS</b>	Robotic Total Station
<b>SNR</b>	Signal to Noise Ratio
<b>TDE</b>	Time Difference Estimation

**UAS** Unmanned Aerial System

**UAV** Unmanned Aerial Vehicle

**UTC** Coordinated Universal Time

**VRS** Virtual Reference Station

**WGS84** World Geodetic System 1984

# Contents

<b>1</b>	<b>Introduction</b>	<b>1</b>
1.1	Motivation . . . . .	1
1.2	Used instruments and software . . . . .	2
1.3	Goals of this thesis . . . . .	3
<b>2</b>	<b>Description of the system AIBot X6 V2 and the software AIProFlight</b>	<b>4</b>
2.1	Hardware - AIBotix AIBot X6 V2 . . . . .	4
2.2	Software - AIBotix AIProFlight . . . . .	5
2.3	Data acquisition and proposed workflow by AIBotix . . . . .	6
2.4	Relevant legal guidelines for UASs in Austria . . . . .	7
<b>3</b>	<b>Accuracy Investigation of the UAS trajectory</b>	<b>9</b>
3.1	Measurement setup and processing approach . . . . .	9
3.2	Synchronisation of the GPS-time and the local RTS-time . . . . .	12
3.2.1	Internal time drift compensation of the RTS . . . . .	12
3.2.2	Time difference estimation by cross correlation . . . . .	13
3.2.3	Accuracy and conclusion . . . . .	14
3.3	Alignment of the GNSS trajectory and the RTS trajectory . . . . .	16
3.3.1	Transformation of the local RTS measurements to WGS84 . . . . .	16
3.3.2	Transformation of the GNSS measurements to the sensor position . . . . .	18
3.4	Results . . . . .	29
3.4.1	Ideal conditions - no obstruction of the GNSS signals . . . . .	29
3.4.2	Problematic conditions - partial obstruction of the GNSS signal . . . . .	34
<b>4</b>	<b>Accuracy investigation of points, measured from the UAS</b>	<b>39</b>
4.1	Measurement setup and processing approach . . . . .	39
4.1.1	Description of the flight area . . . . .	39
4.1.2	Description of the points of interest . . . . .	40
4.1.3	Processing approach . . . . .	41
4.2	Results . . . . .	45
4.2.1	Point Cloud Comparison . . . . .	45
4.2.2	Accuracy of Single Point Positions . . . . .	47
4.2.3	Accuracy of deduced Values . . . . .	50
<b>5</b>	<b>Conclusion and Outlook</b>	<b>53</b>
	<b>References</b>	<b>55</b>
<b>A</b>	<b>Results of experiments under ideal GNSS conditions</b>	<b>57</b>
<b>B</b>	<b>Workflow in Inertial Explorer</b>	<b>60</b>
<b>C</b>	<b>Processing Reports from Agisoft PS</b>	<b>63</b>
C.1	Processing Report from Agisoft PS using the conventional approach . . . . .	63
C.2	Processing Report from Agisoft PS using the novel approach . . . . .	69

# 1. Introduction

## 1.1 Motivation

Over the last years, Unmanned Aerial Systems (UASs) also commonly known as unmanned aerial vehicles or drones, have become more and more popular in many fields. They have become standard equipment in filmmaking and are used for inspecting high rise structures such as wind turbines or power lines. However, the technology does not seem to have found its way into standard geodetic applications yet. One of the reasons for this certainly constitutes the tight regulations [5] on flight permission in populated areas. But also accuracy and efficiency are common issues. AIBotix sets out to tackle one of this issues, namely the efficiency.

Their product, the AIBot X6 V2 can be equipped with a NovAtel GNSS unit containing a geodetic GNSS antenna and receiver. This allows for a novel approach, i.e. directly georeferencing the pictures as opposed to the conventional approach using ground control points (GCPs) for georeferencing. The placement of the GCPs, as well as their measurement in both, the object coordinate system and the image coordinate system is very time consuming. Also, it is not always possible to place GCPs in the scene due to selective accessibility of some measurement areas.

The Institute of Applied Geosciences at Graz University of Technology faces exactly this problem when investigating rock faces. Figure 1–1 exemplary shows two of their projects, where the placement of GCPs constitutes a problem.



**Figure 1–1:** Projects of the institute of Applied Geosciences: Upper Styria (left), and East Styria (right), pictures are provided by Scott Kieffer.

In both examples depicted in figure 1–1, the placement as well as the measurement of GCPs in the scene is very difficult, and potentially dangerous to the surveyor.

The novel approach (i.e. directly georeferencing the pictures using relative GNSS positioning techniques) could remedy this problem, as GCPs would no longer be necessary to determine georeferenced coordinates of object points on the ground. However the influence on the accuracy of the object points using the novel approach remains unknown,

and should be determined in the course of this thesis. The accuracy of the system, using the novel approach is essential in finding possible applications for this faster and more convenient workflow.

## 1.2 Used instruments and software

To assess the accuracy of the novel approach, a relatively large set of instruments and software were used. The used instruments can be classified into two groups, i.e. the instruments necessary for pursuing the novel approach itself, and the instruments necessary for the verification of the results from the novel approach. Table 1.2 shows the used instruments of both groups.

**Table 1–1:** Used instruments

	Type	Instrument	Serial Number	Usage
Application of the novel approach	AIBotix AIBot X6 V2	UAS	0454 2015	carry the camera, the prism and the GNSS Module
	NovAtel GNSS Module	GNSS Module	0157 2016	receive, store and process GNSS raw- and correction data
	Dell Latitude D820	Laptop	CN-0JF242-48643-66R-0553	communication with the UAS via AIProFlight
	EPL5	Camera	V4H001654	take pictures to trigger events in the UAS - logfile
		12mm Obj.	ABR003142	
	Satel Compact Proof IP67	radio modem	1622000169	receive correction data from base station
	WI232	radio modem	no serial number	send correction data to UAS
Leica GS16	GNSS Antenna with integrated Receiver	3242614	base station	
Verification of results	Leica MS60	RTS	882001	measure transformation and object points and track the UAS
	Leica GS15	GNSS Antenna with integrated Receiver	1500527	measure transformation- and object points
	Leica CS20	Field Controller	2472300	control of GS16 and GS15
	Lenovo ThinkPad W541	Laptop	R9-OHFPPV 15/09	control of the RTS via GeoCom

The same classification into components that are necessary for pursuing the novel approach itself, and components that are necessary for the verification of the results from

the novel approach can be done for the used software, which is presented in table 1–2.

**Table 1–2:** Used software packages

	Software	Version	Usage
Application	AIBotix AIProFlight	2.9.0.37	see section 2.2
	NovAtel Inertial Explorer	8.60.6717	post processing of the GNSS trajectory
	Agisoft PhotoScan Professional	1.2.6, build 2834	alignment of the photos and calculation of the point cloud
	Matlab	R2016a (9.0.0.341360)	alignment of the trajectories and analysis of the differences
Verification	Leica Infinity	2.1.0, build 2640	processing of local total station measurements
	3dReshaper	13.1.24994.0	preparation of the point clouds and slope calculation
	CloudCompare	2.8.1	comparison of the point clouds
	Google Earth Pro	7.3.0.3832	visualisation of the trajectories

### 1.3 Goals of this thesis

The main goal of this thesis is to assess the accuracy of object points, determined from a purely air based approach. This means, that no ground access to the measurement area is required as the georeferencing is done solely on basis on the GNSS positions of the taken pictures. Also the achievable accuracy of the sensor position (UAS-trajectory) using this approach will be investigated. This was done under ideal GNSS conditions, i.e. no signal obstruction, as well as under problematic GNSS conditions, i.e. signal obstruction by a line of trees.

## 2. Description of the system AIBot X6 V2 and the software AIProFlight

### 2.1 Hardware - AIBotix AIBot X6 V2

The AIBotix AIBot X6 measures 96 cm x 105 cm x 39 cm and weighs 3.4 kg without any payload. The maximum takeoff weight amounts to 6.6 kg<sup>1</sup>. The UAS consists of two components, the vehicle and the platform. The vehicle consists of the upper part of the UAS with the GNSS unit, an Inertial Measurement Unit (IMU), the storage, the radio module and the motors and rotors. The platform carries the payload e.g. a camera, a prism. It is rigidly connected to the vehicle, but can rotate around its roll axis and its pitch axis. Thus the yaw of the platform is always equal to the yaw of the vehicle, while roll and pitch of the platform are set to compensate roll and pitch of the vehicle yielding a horizontal platform. Figure 2–1 shows the UAS and its components.

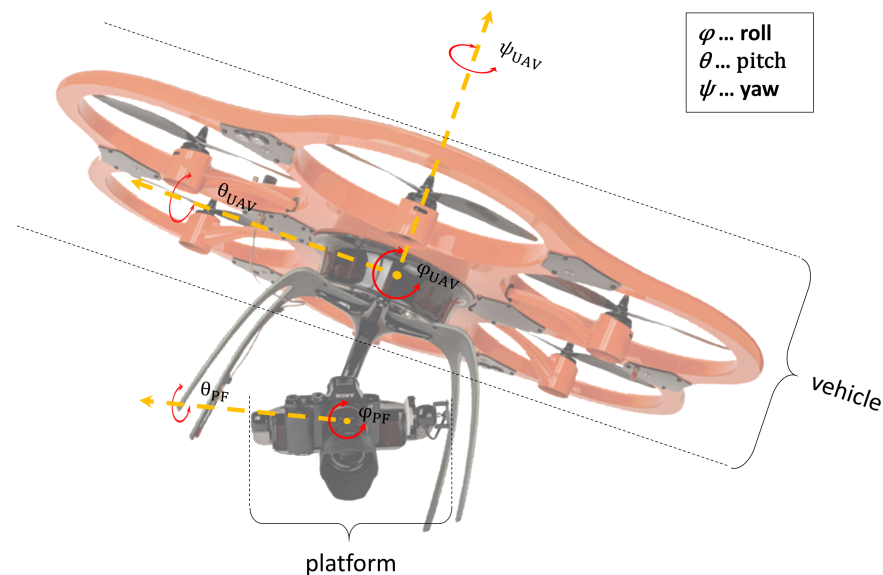


**Figure 2–1:** AIBot X6 V2 with camera and prism payload on platform.

A NovAtel GNSS unit with an antenna of the type GPS-703-GGG [18] can be attached to the vehicle. This unit is capable of receiving and processing satellite signals from GPS, GLONASS, Beidou, and Galileo. In addition, correction data from a base station or a real time positioning service can be received and integrated in an On The Fly (OTF) solution. Besides the geodetic receiver, another conventional GNSS receiver is integrated in the X6 system. This receiver is used for rough positioning, in case that the geodetic receiver is not attached.

Further information about the parts and the proper use of the X6 can be taken from the user manual [2].

---

<sup>1</sup>This includes batteries (0.6 kg), maximum payload weight on the camera gimbal (2.0 kg) and maximum payload weight for the on-top mount (0.6 kg)

## 2.2 Software - AIBotix AIProFlight

AIProFlight is the software that comes with the AIBot X6. Its functionality can be summarised in three main tasks. These are:

1. upload of flight parameters and flight plan to the UAS before the flight
2. passing on GNSS correction data to the UAS during the flight
3. calculating the sensor position from the GNSS measurements and the logfile after the flight

The flight parameters include values like the flight altitude, the platform orientation and the trigger interval for the camera. The flight plan is represented by waypoints, that define the path which the UAS should follow. Once uploaded, the flight plan can be executed. Therefore, the conventional GNSS receiver that is integrated in the X6's frame is used to position the UAS. For this, AIProFlight does not have to be connected to the UAS.

If the NovAtel unit is attached, it is used for positioning the UAS. To further improve the GNSS solution, correction data from a local base station or a real time positioning service can be used. As the OTF processing takes place on the NovAtel unit itself, the correction data must be streamed to the UAS. A real time data link can be established by attaching a sending radio module to a laptop, and a receiving antenna to the UAS. AIProFlight, which runs on the laptop, handles the data stream to the UAS. When using a local base station, another receiving module must be connected to the laptop. When using the correction data from a real time positioning service, the laptop must be connected to the internet.

If the position of the sensor is of interest, the photos must be geotagged. AIProFlights function *Geotagging* calculates the sensor position on the platform from the GNSS receiver position in the vehicle and writes the respective position to each taken picture. The inputs for this transformation are the coordinates of the GNSS receiver, the orientation of UAS and platform, the precise event timestamp (PET), and the sensor position on the platform. The coordinates of the GNSS receiver can either come from the OTF solution, or from a GNSS solution that was calculated using a third party software in post processing. The orientation of UAS and platform, as well as the PET are stored in a binary logfile that is written by the X6. The platform position of the sensor is measured and put in manually. The process of geotagging yields georeferenced pictures, as well as a \*.csv file that contains the picture coordinates as a list.

Further information about the software AIProFlight can be taken from the user manual [3].

## 2.3 Data acquisition and proposed workflow by AIBotix

The calculation of global point coordinates from taken pictures requires the knowledge of inner and outer orientation of the taken pictures. The inner orientation is usually known beforehand from camera calibration. One way to determine the outer orientation is to estimate it in a bundle block adjustment together with the object points themselves. This requires known global coordinates of GCPs, which can be seen and determined in the pictures.

The geodetic GNSS receiver in the UAS allows for another workflow, i.e. directly determining the position of the pictures by means of GNSS measurements. Only the orientation of the pictures would then be determined in the bundle block adjustment from matching points in different pictures. The global coordinates of the matching points do not have to be known. Both approaches are schematically depicted in figure 2–2.

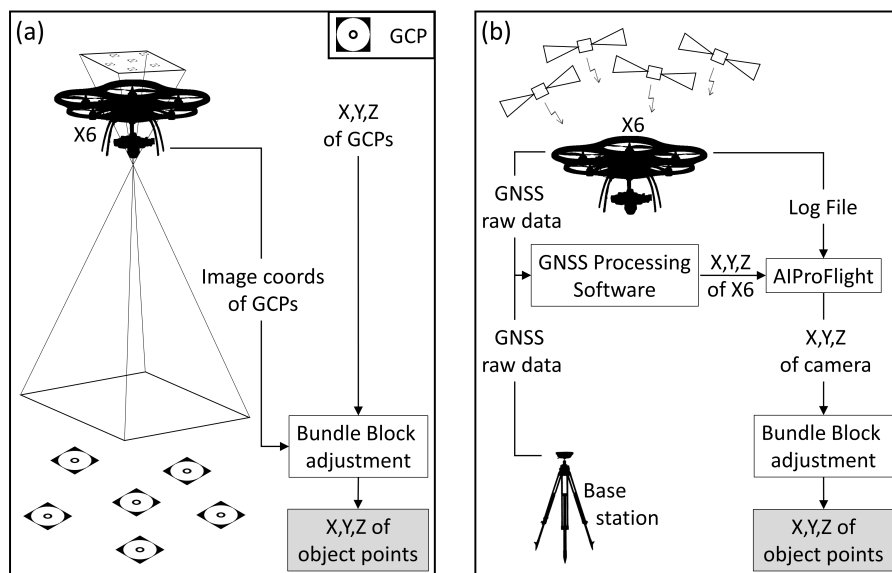


**Figure 2–2:** Approaches to determine global coordinates of object points from aerial photographs: a) conventional approach: using GCPs, and b) novel approach: using well established GNSS relative positioning techniques.

Figure 2–2 (a) shows the conventional approach for airborne photogrammetry using GCPs. The image coordinates of the GCPs, as well as the coordinates in the object coordinate system serve as input for a bundle block adjustment. While the image coordinates can be measured directly in the images, the coordinates in the object system must be measured in the field e.g. by tachimetry or GNSS positioning. Among others, the estimated parameters of the bundle block adjustment are the 3D-coordinates of the object points in the object coordinate system. For more detailed information concerning bundle block adjustment refer to Luhmann 2011 [15] (p. 229-265).

Figure 2–2 (b) shows one of the workflows proposed by AIBotix, which makes use of the integrated geodetic GNSS receiver within the AIBot X6. This GNSS receiver as well as a local base station on the ground record raw data during the flight. The data

from both receivers is then processed in a 3rd party software<sup>2</sup> using relative processing techniques. This yields a precise trajectory (PP-coordinates) of the GNSS receiver in the X6. Please note, that the trajectory of the X6 can also be calculated in real time. Therefore, correction data from the local base station or from a real time positioning service (e.g. APOS, EPOSA, Leica SmartNet, Trimble VRS Now) can be streamed to the UAS using a laptop and AIBotix's software AIProFlight. The PP-coordinates as well as a log-file from the X6 are fed into AIProFlight which calculates coordinates of the camera at every point in time, when a picture was taken. The picture coordinates are written directly to the picture using the Exif standard [4]. Employing this data in a bundle block adjustment yields the 3D-coordinates of the object points in the object coordinate system.

To associate the GNSS position with a taken picture, the *Geobox* is mounted on the hot shoe of the camera. Every time a picture is taken, a timestamp (PET) as well as the current angle readings of the vehicle and the platform are written to a binary log-file. From the GNSS positions, the PET, the angle readings of UAS and platform and the location of the payload on the platform, the global payload position can be calculated every time a picture is taken. These points in time are called *events*. A comparison of the UAS trajectory to a reference trajectory (of a point on the platform) is only possible at the times of the events.

### 2.4 Relevant legal guidelines for UASs in Austria

According to §24f and §24c of the Austrian aerospace law (Luftfahrtgesetz), a UAS specifies as such, if it is not used for flight purposes only, but if it is used to pursue another purpose. One purpose would be the recording of pictures or videos. But also if an aerial system is used for fertilizing fields in agriculture it would specify as an UAS or a drone. Drones below a weight of 250 grams and a maximal flight height of 30 meters specify as toys and therefore need no official admission. Drones that exceed these specifications fall into class 1 Unmanned Aerial Systems and need admission by the Austrian aeronautical authority, i.e. Austro Control. The AIBotix X6 V2 specifies as a class 1 UAV.

The admission of flights with a specific drone depends on two factors, namely the weight of the drone, and the area over which the flight should take place. Table 2–1 shows the respective admissions required for different values of the two factors.

---

<sup>2</sup>The raw data recorded by the NovAtel Unit in the X6 is stored in the NovAtel internal .AFL format. This format can only be read by Waypoint products, and cannot be correctly converted to the RINEX format at the time of this thesis (August 2017). I used Inertial Explorer, version 8.60.6717.

**Table 2–1:** Mandatory admissions for class 1 drones

	I uncultivated area	II unsettled area	III populated area	IV densely populated area
takeoff weight $\leq 5$ kg	A	A	B	C
takeoff weight $\leq 25$ kg	A	B	C	D
takeoff weight $\leq 150$ kg	B	C	D	D

The AIBotix X6 weighs a maximum of 6.6 kg as described in section 2.1. The Institute of Applied Geosciences holds an admission of category A, making it only possible to fly over uncultivated areas. Uncultivated areas are defined as areas without any buildings whatsoever, and no human beings located within the area. These regulations must be taken into consideration when choosing the flight area for the test flights. Further and more detailed information on drone regulations in Austria can be taken from Austro Controls homepage [5], as well as the homepage of the Federal Ministry for Traffic, Innovation and Technology [1].

# 3. Accuracy Investigation of the UAS trajectory

## 3.1 Measurement setup and processing approach

To investigate the accuracy of the GNSS-based trajectory of the UAS, a "true" reference trajectory is necessary. This "true" reference trajectory is measured by means of a robotic total station (RTS). In this thesis, a Leica MS60 is used, however every RTS capable of automatically tracking a prism can potentially be used.

The RTS tracks a Leica GRZ101 mini-360° prism, which is attached to the platform of the UAS. Figure 3-1 schematically shows the configuration of the measurements.

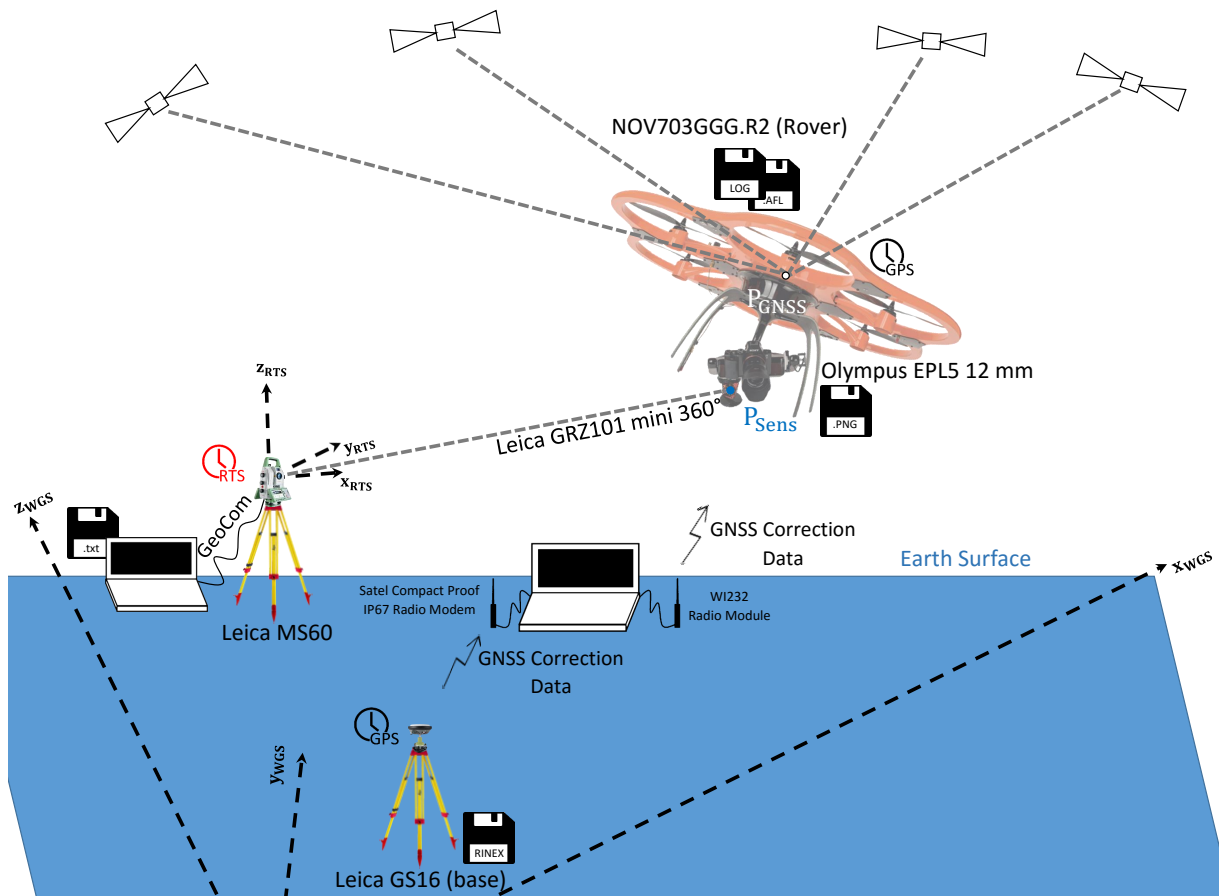


**Figure 3-1:** Measurement setup during the experiments to investigate the accuracy of the UAS trajectory.

The measurements in this setup yield three trajectories, one reference trajectory, and two test trajectories, i.e. the PP-test trajectory and the OTF-test trajectory.

The reference trajectory is calculated from the RTS (Leica MS60) measurements. The RTS is controlled by a laptop, running a GeoCom script that makes the RTS dynamically lock on to, and track the GRZ101 mini 360° prism, i.e.  $P_{Sens}$ . The measured values, as well as the RTS-internal timestamp, inclination data of the RTS and internal temperature are written directly to an ASCII (American Standard Code for Information Interchange)

textfile on the laptop. From the measurements in this textfile (the RTS measurements) we calculate coordinates of  $P_{\text{Sens}}$  in the local horizontal system of the RTS. The timestamp of this coordinates is given in milliseconds precision and refers to the point in time, where the instrument is switched on.

The test trajectories are calculated from GNSS measurements using relative positioning techniques. The NovAtel receiver on board of the UAS functions as the rover, whereas the ground based Leica GS16 functions as the base station. The base station coordinates are measured beforehand by means of connecting to the real time positioning service EPOSA. To enhance the positioning accuracy of a single receiver, EPOSA offers among others, the network method *Virtual Reference Station* (VRS). Further information on the services of EPOSA can be taken from their information sheet [8]. This method was used to determine the position of the base station (Leica GS16). The base station, as well as the rover record GNSS raw data. Using a 3rd party software, this data is used in post processing to calculate the trajectory of the rover in the global WGS84 system. The timestamp of the coordinates refers to 00:00:00 UTC on January 6, 1980 (GPS time). This trajectory will be referred to as the PP-R-trajectory.

The same principle can also be applied to a real time approach. Therefore, the base station is set up to send out correction data via an internal radio module. This correction data is received by a *Satel Compact Proof IP67 Radio Modem*, that is connected to a laptop via a serial port. Note that this is not the same laptop that is used to control the RTS. Also connected to the receiving laptop is a *WI232 Radio Module*, that passes the correction data on to the NovAtel unit on board of the UAS using AIProFlight (see section 2.2). The NovAtel unit is capable of processing the received GNSS data as well as the correction data on the fly. These coordinates (OTF-R-trajectory) are written to a binary logfile (\*.aiLogX) that can be downloaded from the UAS after the flight. As the PP-R-trajectory, the OTF-R-trajectory also refers to WGS84 in GPS time.

Both trajectories (PP-R and OTF-R) however describe  $P_{\text{GNSS}}$  whereas the reference trajectory describes  $P_{\text{Sens}}$ . The trajectories, that describe  $P_{\text{Sens}}$ , but are calculated from the GNSS measurements are the desired test-trajectories PP-test and OTF-test. To calculate these trajectories from the trajectories PP-R and OTF-R, a series of transformations both in space and in time must be carried out. Also the reference trajectory must be transformed to WGS84 and GPS time. The procedure for aligning all three trajectories is outlined in figure 3–2. The precise steps are described in the sections below.

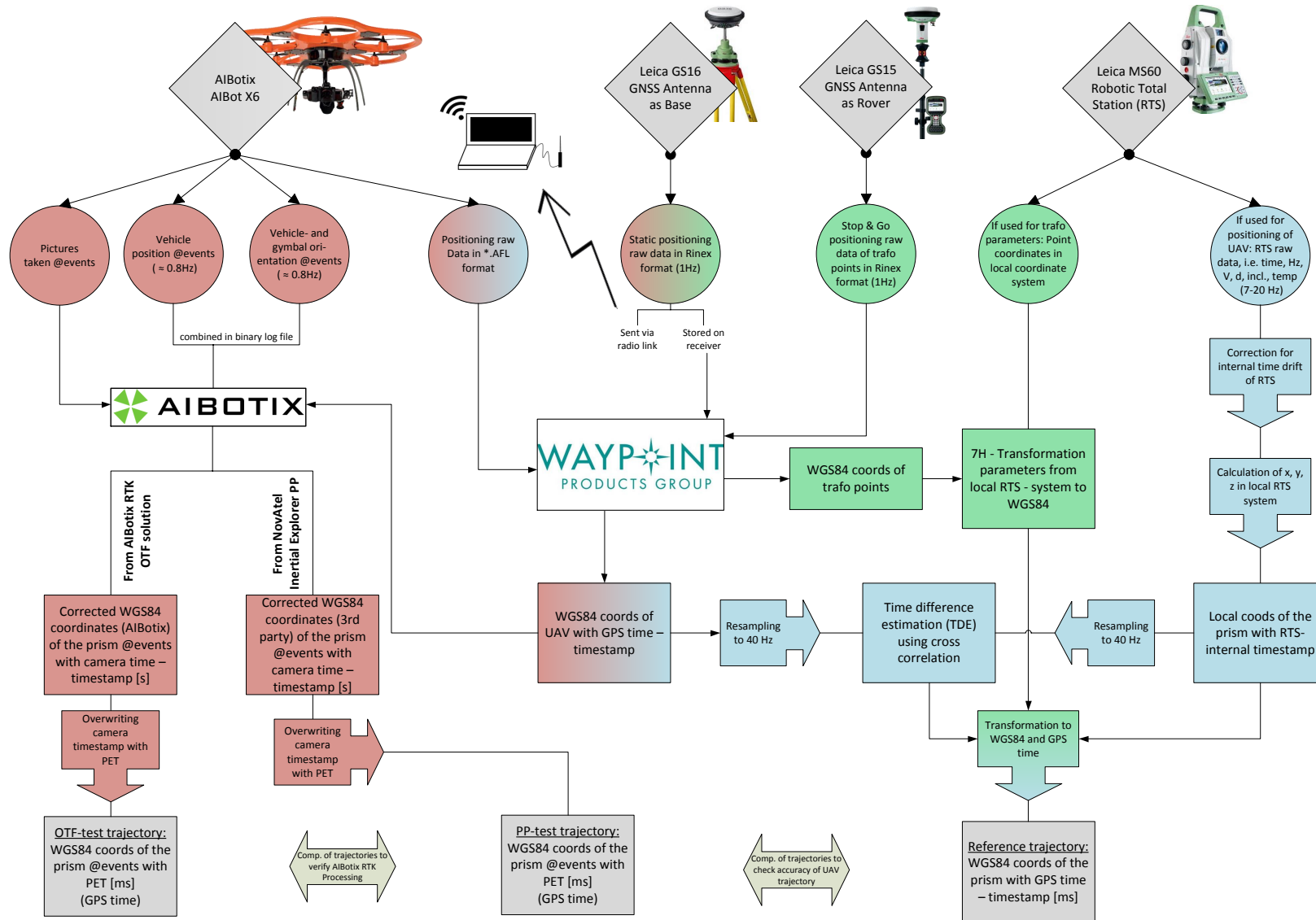


**Figure 3–2:** Procedure for aligning the reference trajectory, the OTF-test trajectory and the PP-test trajectory to each other. The three colours correspond to the main steps of alignment procedure as follows: Blue indicates the synchronisation of the GPS-time and the local RTS-time, green indicates the transformation of the RTS measurements to the global WGS84 system and red indicates the transformation of the GNSS trajectory to the prism on the platform. The circular fields indicate measured datasets, the pointer-fields indicate operations and the rectangular fields indicate resulting datasets. The diamond shapes indicate the sensors.

## 3.2 Synchronisation of the GPS-time and the local RTS-time

The timestamp of the single measurements is used for identifying two corresponding measurements in the different trajectories. Therefore, synchronising the local time (used by the RTS) to the GPS-time (used by the UAS) is crucial for being able to meaningfully compare points of the reference trajectory and the test trajectories.

As the UAS is in motion, an error in the time synchronisation leads to a mismatch of the points of the trajectories and thus looks like a position error. At an average velocity of  $2 \text{ ms}^{-1}$ , a synchronisation error as small as 10 ms corresponds to a position error of 2 cm! Considering the expected accuracy of relative GNSS positioning techniques is also in the scope of a few centimetres, the maximum tolerable position error from the synchronisation is defined to be 4-6 mm. This corresponds to a maximum tolerable synchronisation error of 2-3 ms.

### 3.2.1 Internal time drift compensation of the RTS

Gojic 2016 [10] (p.21-57) found in his thesis, that Leicas MS60 internal time shows a temperature dependent drift in the dimension of 56 to 59 ppm, for temperatures of 20 and  $40^\circ\text{C}$  respectively. This time drift corresponds to an error in time of about 200 ms/h, and therefore needs to be considered to stay below the demanded maximum tolerable synchronisation error (section 3.2).

The calibration function for Leicas MS60 internal time, found by Gojic 2016 [10] is depicted in figure 3-3.

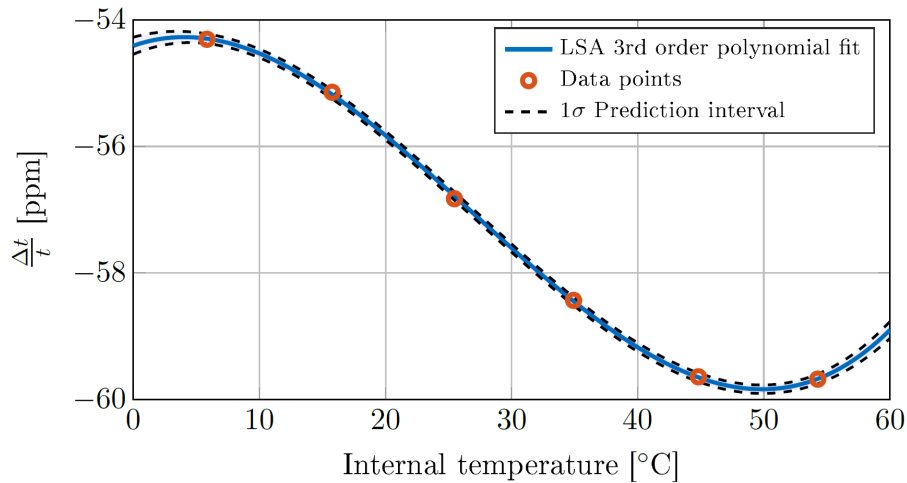


**Figure 3-3:** Leica MS60 internal time drift calibration function [10]

This function delivers the drift rate in ppm after (3-1).

$$\frac{\Delta t}{t} = a_0 + a_1 T_{\text{Int.}} + a_2 T_{\text{Int.}}^2 + a_3 T_{\text{Int.}}^3. \quad (3-1)$$

with the parameters

$$\begin{aligned}
 a_0 &= -54.4086 & [ & ] \\
 a_1 &= 0.0698 & [^\circ\text{C}^{-1}] \\
 a_2 &= -0.0093 & [^\circ\text{C}^{-2}] \\
 a_3 &= 0.0001 & [^\circ\text{C}^{-3}]
 \end{aligned}$$

The calibrated internal RTS time can then be calculated from the measured internal RTS time and the drift rate after (3-2).

$$t_{\text{Int.}}^{\text{calibrated}}(i) = t_{\text{Int.}}^{\text{calibrated}}(i-1) + (\Delta t_{\text{Int.}}^{\text{measured}}(i) - \frac{\Delta t}{t}(i) \cdot \Delta t_{\text{Int.}}^{\text{measured}}(i)) \quad (3-2)$$

Every timestamp must be corrected by the function above before synchronising the GPS-time and the internal time.

### 3.2.2 Time difference estimation by cross correlation

The time used by the MS60 refers to the point in time, when the instrument is switched on. When rebooting the instrument, the time also restarts. Therefore, an estimated time delay between the internal MS60 time and the GPS time is only valid for as long as the MS60 is not restarted.

The synchronisation is carried out by means of cross correlation between the two trajectories (GPS and RTS). Multiple peaks are therefore generated by increasing and decreasing the height of the UAS while tracking the attached prism with the RTS. The resulting trajectories will both show the generated peaks in the height component. However the timestamps of the two trajectories as well as the sampling frequency are not equal. Figure 3-4 shows the sampling frequency of the different datasets.

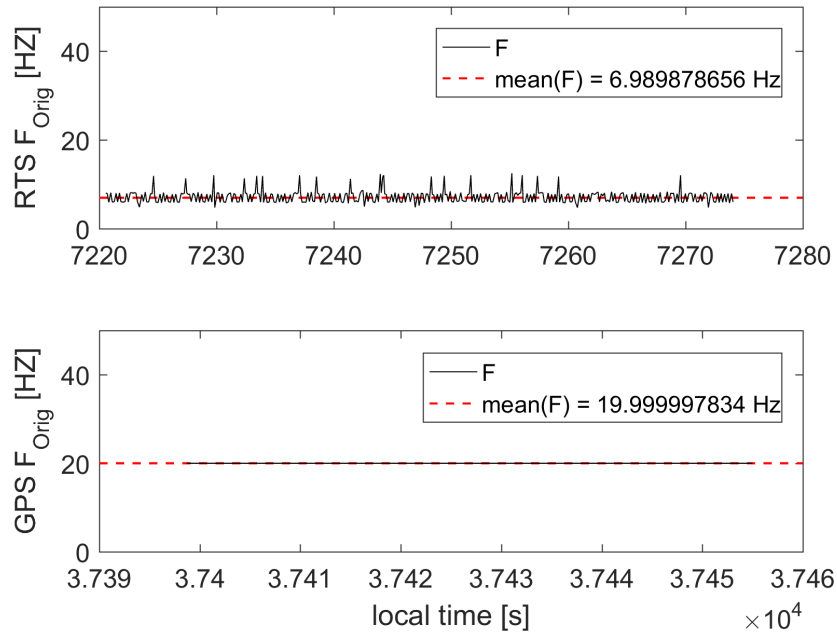


**Figure 3-4:** Sampling frequency of the RTS observations at the top and of the GPS observations at the bottom.

The RTS measurements have an average sampling frequency of about 7 Hz while the GPS data is obtained at a rate of about 20 Hz. Using shape-preserving piecewise cubic

interpolation, the datasets are resampled to 1000 Hz, while also eliminating sharp edges in the datasets.

The lag between corresponding peaks can now be determined by calculating the cross correlation function (CCF) of the modified datasets. To improve the temporal resolution of the TDE, we used subsample interpolation of the CCF using three-point parabola fitting as described by Wiens and Bradley 2009 [20] (p. 3). Knowing the sampling frequency (i.e. 1000 Hz), the lag can be easily converted to the actual time delay (TD) after (3–3).

$$\text{TD} = \frac{\text{lag}}{F_{\text{sampling}}} \quad (3-3)$$

### 3.2.3 Accuracy and conclusion

The accuracy of this procedure was evaluated, by carrying out the procedure described above twice (or in case of the last experiment thrice). Once before the start of the actual experiment, and once at the end. The TDEs of the two procedures are depicted in table 3–1. Note that the values given here refer to 00:00:00 h of the day where the experiment was carried out.

**Table 3–1:** TDE of the main experiments. Note, that experiment 2 (2017/07/11) failed due to an error of the camera. Hence, no trajectory of the prism could be calculated and the TDE in this case remains unused. Nevertheless, the synchronisation procedure is complete and therefore depicted here.

Experiment	ID	sync. proc. no.	TDE <sub>local</sub>	$\Delta\text{toSP}_1$ [ms]	mean(TDE <sub>local</sub> )
2017/03/16 GNSSShading	1	1	8h 23m 0.927s	0	8h 23m 0.927s
		2	8h 23m 0.927s	0	
2017/07/11 SensorOffsets	2	1	6h 5m 28.184s	0	6h 5m 28.176s
		2	6h 5m 28.168s	-16	
2017/07/20 SensorOffsets	3	1	9h 29m 8.283s	0	9h 29m 8.283s
		2	9h 29m 8.287s	4	
		3	9h 29m 8.279s	-4	

Using the procedure described above, the aspired accuracy of 2-3 ms could only be reached in the first experiment. This is the result of bad correlation properties of the periodic signal generated by the multiple peaks. Figure 3–5 shows the overlaid signals (i.e. the height) of the RTS and the GNSS trajectory, as well as their CCF and a detail of the CCF at maximum correlation.

### 3. ACCURACY INVESTIGATION OF THE UAS TRAJECTORY

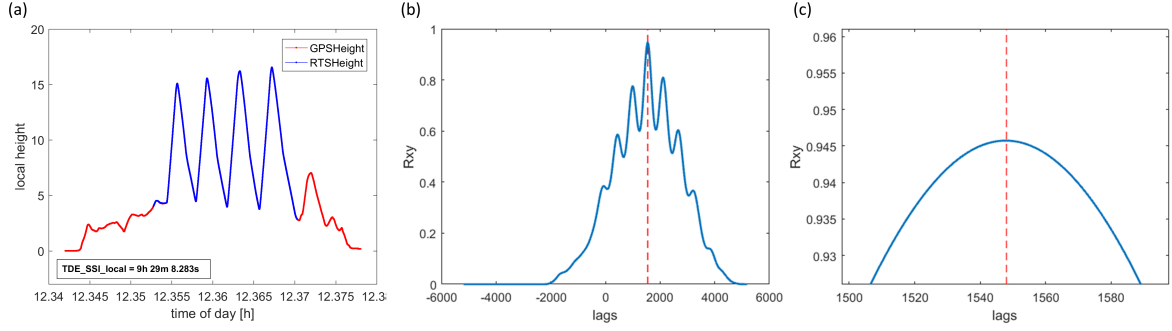


**Figure 3-5:** Experiment 3, sync.proc. no. 3: (a) aligned signals (RTS data in blue, and UAS data in red), (b) CCF of the signals and (c) detail of the CCF at maximum correlation coefficient.

As the signal is periodic, the CCF is periodic as well. As can be seen in figure 3-5 (c), the maximum peak is relatively flat. This is the result of the low velocity of the rise (up to  $3 \text{ ms}^{-1}$ ) and the decline (up to  $2 \text{ ms}^{-1}$ ) of the UAS. The properties of this specific CCF make identifying the exact time delay difficult. An error in the estimated time delay, results in a position matching error between the two trajectories, as described in section 3.2. The position error resulting from the matching error is proportional to the current velocity of the UAS though. This allows for an independent check of the TDE by looking into the dependency between position error and velocity of the UAS. To demonstrate this property, figure 3-6 shows the results of experiment 3, once with the actually calculated time delay (left), and once with a manually biased time delay (by 10 ms, right).

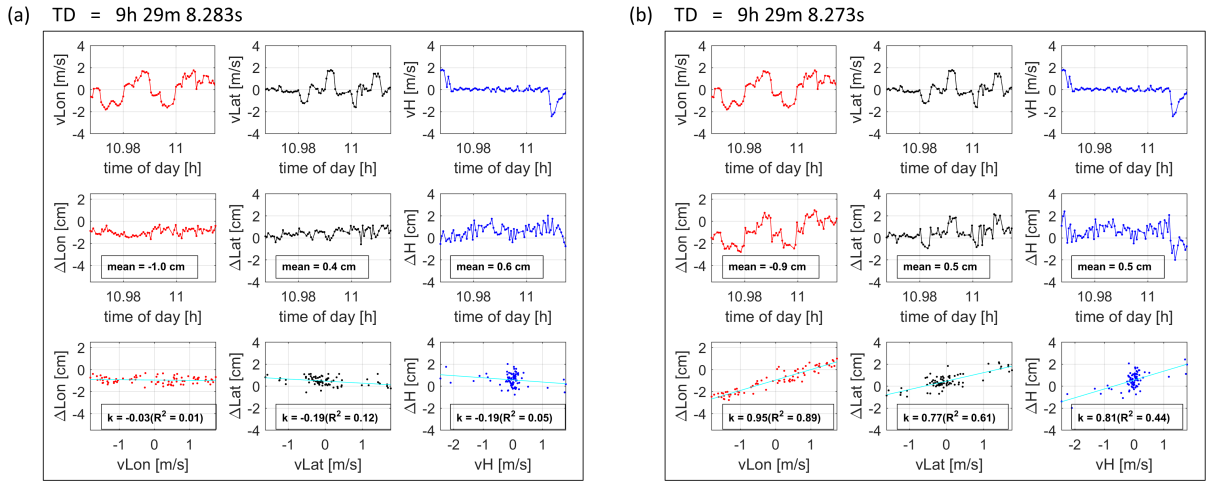


**Figure 3-6:** Results of experiment 3, (a) with the calculated time delay of 9h 29m 8.283s, and (b) with the manually biased time delay of 9h 29m 8.273s (-10 ms). Values in the directions longitude (red) latitude (black) and height (blue): Velocity over time on the top, position error over time in the middle and position error over velocity at the bottom.

In the bottom row of figure 3-6, the position error is depicted over the velocity. In figure 3-6 (b), the data in the different coordinate directions shows trends between 0.77 and 0.95 cm per  $\text{ms}^{-1}$ , which roughly corresponds to the distance the UAS travels in 10 ms i.e. 1 cm. In figure 3-6 (a) (TDE without manual alternation), the position error shows no dependency on the velocity. This indicates, that the calculated time delay is correct.

Retrospectively speaking, an easier and more robust time synchronisation procedure could have been ensured, by generating a signal with better correlation properties. This can be accomplished by two measures concerning the generation and measurement of the trajectories.

1. Lienhart et al. showed in 2016, that 3d-measurements with the MS60 are potentially possible at a frequency of up to 25 Hz [14] when controlling it by GeoCom. When simultaneously streaming a video to the Laptop however, the average measurement frequency drops to about 7 Hz. A lower frequency causes a lower resolution of the estimated time delay. No video should therefore be streamed from the RTS camera to the GeoCom laptop during the synchronisation procedure.
2. The height increase and decrease of the UAS is limited by its rotor power and safety guidelines respectively. Therefore, the creation of a sharper peak is not possible by the UAS itself. A sharp peak could however be generated, by simply altering the height of the UAS in another, faster way. One possibility would be, to hold the UAS and rapidly moving it from chest height over ones head and down again.

Both of these measures would allow for the generation of one sharp peak with better correlation properties, hence making the TDE more accurate.

### 3.3 Alignment of the GNSS trajectory and the RTS trajectory

The alignment of the GNSS trajectory and the RTS trajectory can be split in two major steps. These are:

1. The transformation of the RTS measurements to the global WGS84 system.
2. The transformation of  $P_{\text{GNSS}}$  (measured by GNSS) to  $P_{\text{Sens}}$  (see figure 3–1).

Following sections will describe the two steps in more detail. Please refer to section 3.1 for informations about the measurement setup.

#### 3.3.1 Transformation of the local RTS measurements to WGS84

In general, a transformation from one cartesian coordinate system to another can be defined by 7 parameters which are three shifts, three axis rotations and a scale factor. Hence the mathematical model can be written as

$$\begin{bmatrix} x \\ y \\ z \end{bmatrix}^{(B)} = \begin{bmatrix} t_x \\ t_y \\ t_z \end{bmatrix}^{(B)} + s \cdot R(\alpha_x, \alpha_y, \alpha_z) \cdot \begin{bmatrix} x \\ y \\ z \end{bmatrix}^{(A)} \quad (3-4)$$

The superscripts (A) and (B) indicate coordinates expressed in system A and system B respectively.  $R(\alpha_x, \alpha_y, \alpha_z)$  is a composite rotation matrix consisting of three rotations

$\alpha_x$ ,  $\alpha_y$  and  $\alpha_z$  and  $s$  is a scale factor.  $[t_x \ t_y \ t_z]^T$  is the translation vector between the origins of both systems measured in system B. Further notes on this topic are available in Deakin 2006 [6] (p. 3).

If the transformation parameters are not known a priori, a minimum of 7 coordinate pairs (e.g. 2 points and the height of a third point) must be known in both systems to determine them. Given that the number of known identical points is generally a whole number larger than three, the transformation parameters must be estimated. As commonly used in geodesy, the Gauss-Markov ordinary least squares adjustment model [16] (p. 133-135), is applied. Thus the estimated parameters ( $\hat{x}$ ) can be calculated according to (3-5).

$$\hat{x} = (A^T \Sigma_{ll}^{-1} A)^{-1} A^T \Sigma_{ll}^{-1} l \quad (3-5)$$

The vector  $l$  contains the observations i.e. the coordinates of the measured points in the global system.  $\Sigma_{ll}^{-1}$  contains the a-priori variances of said observations, and the matrix  $A$  describes the functional relationship between observations ( $l$ ) and parameters ( $x$ ) so that following equation holds true.

$$l = Ax + v \quad (3-6)$$

Note, that the coordinates of the measured points in the local system also contribute to the the values in  $A$ . The vector  $v$  represents the residuals of the observations  $l$ . The covariance matrix of the estimated parameters can be calculated after (3-7).

$$\Sigma_{\hat{x}\hat{x}} = \sigma_0 (A^T P A)^{-1} \quad (3-7)$$

with

$$\sigma_0 = \frac{v^T P v}{\text{degree of freedom}}$$

From  $\Sigma_{\hat{x}\hat{x}}$ , the covariance matrix of any point which is transformed to the global system using the parameters in  $\hat{x}$  can be calculated after (3-8)

$$\Sigma_{gg} = A \Sigma_{\hat{x}\hat{x}} A^T \quad (3-8)$$

Note, that  $A$  must be recalculated with the local coordinates of the transformed points.  $\Sigma_{gg}$  contains the variance of the three coordinates of every point in the diagonal. Figure 3-7 shows the Mean Point Error after Helmert (MPE) of one of the transformed trajectories.

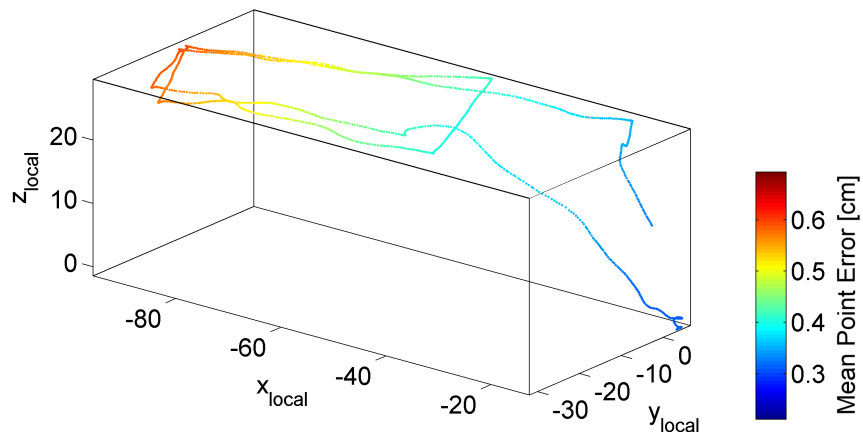
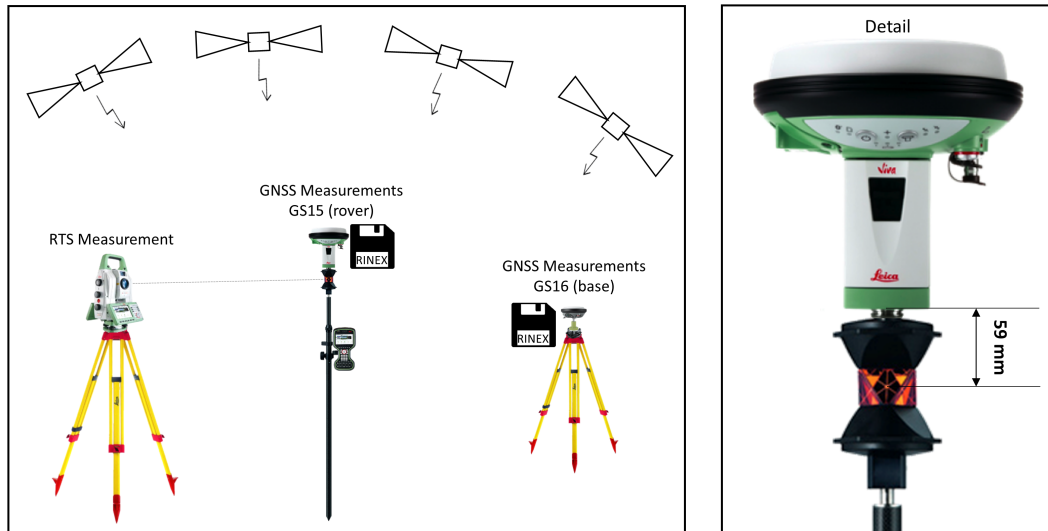


Figure 3-7: Trajectory and MPE of flight 0019.

In this calculation it is assumed, that the coordinates are error free, therefore the accuracy shown here only applies to the transformation itself. The trajectory is shown in the local system. The colour indicates the accuracy of the respective point when transformed from the local to the global system. The accuracy declines proportionally to the distance from the rotation centre, i.e. the origin. This is expected, as the error in the rotation angles scales with the distance. The maximum MPE in all experiments amounts to 6.4 mm, the minimum to 2.0 mm.

In all experiments that were carried out after the scheme depicted in figure 3–1, a minimum of five points were determined in both systems by measuring them with both the RTS (local system) and a Leica GS15 GNSS receiver (WGS84). For each point, 30 GNSS position solutions were calculated, before moving on the the next one. In addition, the measurements by the GS15 are supported by the local base station (i.e. the GS16). This allows for point accuracies of around 1 cm. The simultaneous measurement of a single point by RTS and GNSS was realised by attaching the GS15 to a Leica GRZ122 360° prism, as schematically depicted in Figure 3–8).



**Figure 3–8:** Setup to measure identical points in local and global coordinate system with detail of prism-antenna joint.

Using these identical points as observations in the previously described adjustment, returns transformation parameters that can be employed in (3–4) to transform the measured prism coordinates  $P_{\text{Sens}}$  to the WGS84 system.

#### 3.3.2 Transformation of the GNSS measurements to the sensor position

The GNSS measurements of the UAS do not refer to the position of the prism, but rather to the phase centre of the GNSS receiver ( $P_{\text{GNSS}}$  in figure 3–1). However the reference trajectory refers to the position of the attached prism ( $P_{\text{Sens}}$  in figure 3–1).  $P_{\text{Sens}}$  can be calculated from  $P_{\text{GNSS}}$ , however the calculation requires the following parameters:

- current orientation angles, i.e. roll, pitch and yaw of the UAS as well as roll and pitch of the platform
- rotation centres, to which the orientation angles refer
- translation vector from  $P_{GNSS}$  to  $P_{Sens}$

The current orientation angles are given, every time a picture is taken, i.e. an event occurs. The translation vector could be easily determined once the rotation centres are known, however the rotation centres are not known a-priori and therefore would have to be measured. The measurement of said rotation centres would require serious effort and would not be as accurate as the manufacturers values. Therefore, the manufacturers software AIProFlight [3] (p. 40-45), is used to calculate  $P_{Sens}$  from  $P_{GNSS}$ . More precisely, the function *Geotagging* is used. Using this function, two subjects must be addressed:

- Determination of the precise event timestamp
- Determination of the precise sensor offsets

#### Determination of the precise event timestamp

When using *Geotagging* for the determination of  $P_{Sens}$  from  $P_{GNSS}$ , the timestamp of the events is shown only to seconds precision. One second, at an average velocity of  $2 \text{ ms}^{-1}$  correlates to 2 m uncertainty of a point position in the trajectory. This would not allow for a reasonable comparison to the reference trajectory.

Internally however, the event timestamp is logged with milliseconds precision (AIBotix support 07.04.2017). This precise event timestamp (PET) remains hidden from the eyes of the user, but is used when pursuing the post processing workflow.

In the post processing workflow, rather than using the coordinates of the OTF-GNSS solution from AIProFlight, the coordinates of an externally calculated solution are used. The solution is calculated from the raw GNSS data, that is recorded in the AIBot. These recorded raw data files however are stored in the NovAtel internal, binary data format *.AFL*. To convert *.AFL* files to the open RINEX format, NovAtel offers a conversion tool. However, the tool does not label the recorded L2C data correctly, hence the RINEX files cannot be used for correct processing (NovAtel Support 05/24/2017).

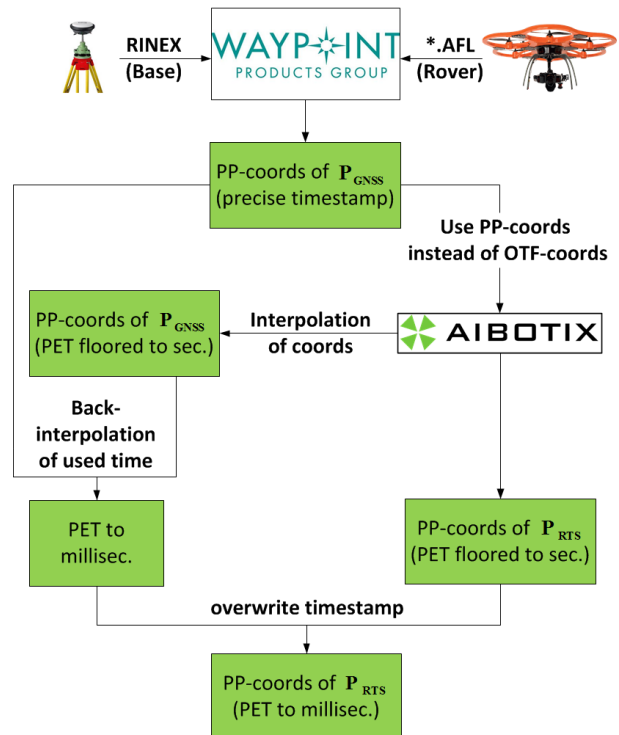


**Figure 3–9:** Concept for determining the PET from the interpolated coordinates in AIProFlight.

To directly process files in the AFL format, a software package of the Waypoint Products Group must be used. We used Inertial Explorer for post processing of the GNSS raw data and thus receiving precise coordinates. Going forward, this externally calculated coordinates (PP-coordinates) can be used in AIProFlight instead of the internally calculated coordinates (OTF-coordinates). In general, the OTF-coordinates and the PP-coordinates are not recorded at the same frequency, hence the timestamps do not match. Therefore, AIProFlight linearly interpolates the given PP-coordinates using the PET (AIBotix Support 07.04.2017). The PET is still not visible for the user, however the interpolated coordinates are. This interpolated coordinates can be used to determine the precise timestamps, which have been used to acquire them from the given PP-coordinates. Figure 3–10 graphically shows the situation for determining the PET.

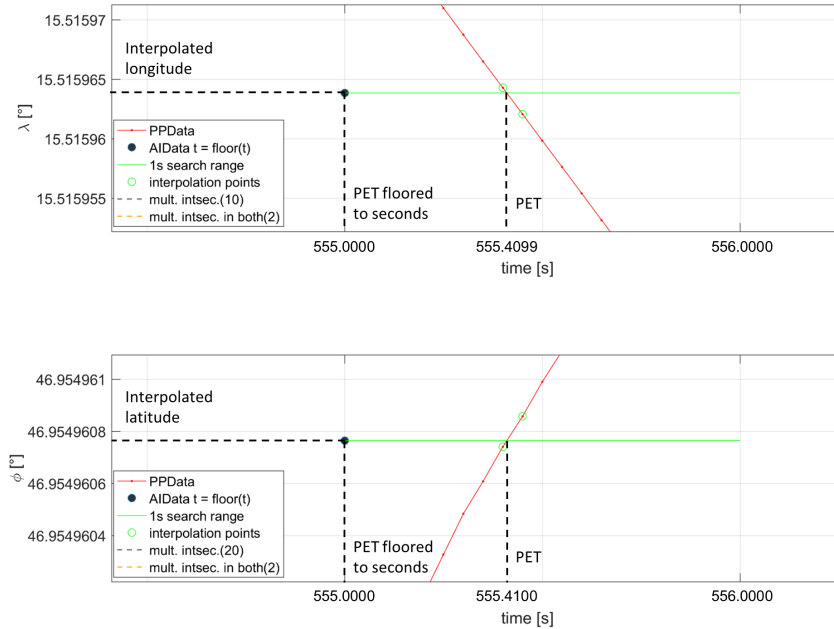


**Figure 3–10:** PET determination using externally calculated coordinates for Geotagging in AIProFlight. The *shown timestamp* ( $t_{\text{show}}$ ) of the event is floored to seconds precision. Therefore, following relation always holds true:  $t_{\text{showed}} \leq \text{PET} < t_{\text{showed}} + 1$  [s]. This defines the search range for the PET with 1 second.

In some instances, multiple intersections of the interpolated coordinate within the 1 second search range occur. If this is the case in only one coordinate direction, the timestamp of the other coordinate direction with a unique intersection is used. If however multiple intersections occur in both coordinate directions i.e.  $\lambda$  and  $\varphi$ , the PET of that specific event cannot be determined and therefore is omitted. This happens when the coordinates do not change or return to the same value within one second e.g. when the UAS is hovering in one place.

The maximum difference between the precise timestamps for one event, acquired independently from the interpolated latitude and the interpolated longitude is 2 ms. This can

however be considered an outlier, as 95 % of the differences are below 350 ns. The reason for an outlier like that can be a disadvantageous intersection angle. After eliminating outliers, the remaining differences are normally distributed with  $-13 \text{ ns} \leq \mu \leq 8 \text{ ns}$  and  $51 \leq \sigma \leq 116 \text{ ns}$  (for different experiments). These differences can be neglected due to their small impact on the trajectory i.e.  $< 1 \text{ mm} @ 2 \text{ ms}^{-1}$ .

#### Investigation of the sensor offsets on the platform

For the determination of the sensor position from the GNSS position, the location of the sensor on the platform is (among others) one of the necessary inputs. AIBotix defines this location by three sensor offsets in three coordinate directions, and a reference point on the platform (see [3]). The sensor offsets measured according to the manual for the used prism are depicted in figure 3–11.

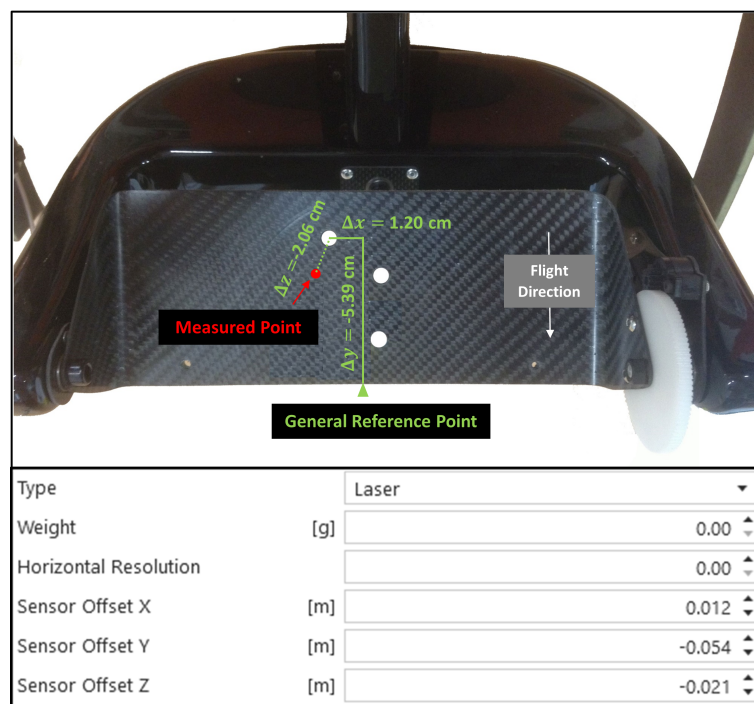


**Figure 3–11:** Sensor offsets to the measured point (i.e. the prism) and definition of a payload in AIProFlight with the measured offsets

When processing different trajectories with this offsets however, systematic differences occurred. This differences lead us to suspect, that the way in which the sensor offsets are specified in the AIProFlight user manual, is not actually the way they are used in the calculation. To verify this suspicion, we carried out an experiment. In the experiment the RTS tracked the UAS, while it flew different paths with changing orientation. The paths as well as the orientation of the UAS and the position of the tracking RTS are depicted in Figure 3–12.

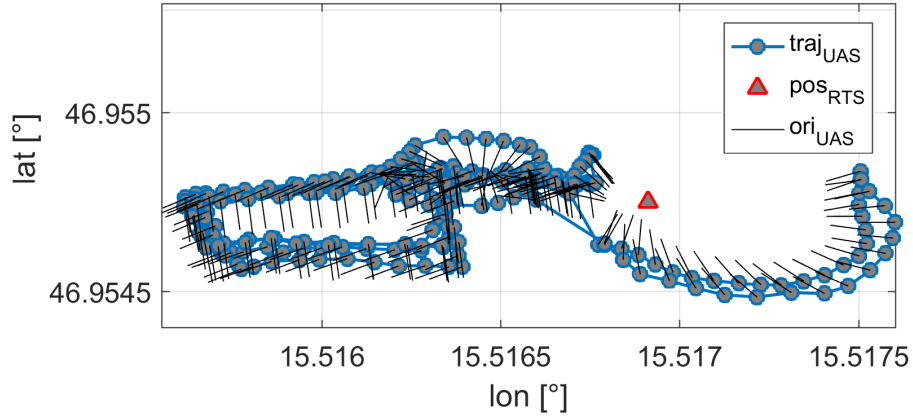


**Figure 3–12:** Trajectory and orientation of the UAS in the described experiment (4 flights) and position of the tracking RTS.

To confirm that the error is a result of the sensor offsets and not of the RTS distance measurement, the UAS flew, among other trajectories, two separate circles. One circle with the RTS in the center, and one circle with the RTS not in the center. These two different setups would show different patterns in the coordinate differences to the RTS measurements, if a systematic offset in the RTS distance measurement causes the error. If the patterns are the same for both circles, it is very likely that they are not caused by a distance measurement error.

If the actual sensor offsets are in fact different from the entered sensor offsets, three possible patterns can result from a comparison to exact reference coordinates when rotating the UAS:

1. A constant offset if the direction of the sensor offset is parallel to the rotation axis
2. A harmonic oscillation if the direction of the sensor offset is normal to the rotation axis
3. A combination of 1. and 2. if the direction of the sensor offset is in any other angle to the rotation axis

Option 3 is only presented for the sake of completeness, as only 1. and 2. will be relevant for this case.

Before going into the data of this experiment though, I want to describe possible geometric situations of the reference point, the platform and the yaw-rotation axis of the drone itself. Figure 3–13 shows a schematic outline of the platform with reference point and rotation axis in two different setups. Note that the exact location of the reference point and the rotation axis is unknown, hence this two cases are merely examples for possible locations.

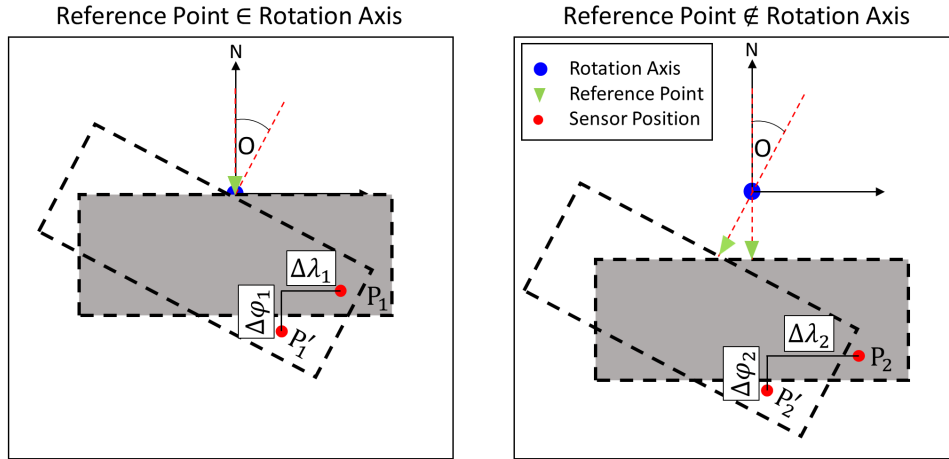


**Figure 3–13:** Different cases of the reference point location with respect to the yaw-rotation axis of the UAS: reference point lying on rotation axis (left), and reference point not lying on the rotation axis (right).

In both figures, the gray rectangle represents the platform of the UAS, the blue point represents the projected yaw-rotation axis of the UAS and the green triangle represents the reference point, to which the sensor offsets refer to.  $O$  is the orientation of the UAS and the dashed rectangle is the platform under this orientation.  $P$  and  $P'$  represent the sensor position when the platform's orientation is 0 (i.e. the platform faces north) and when the platform's orientation is  $O$ . Figure 3–13 left shows the situation in which the reference point lies on the rotation axis, and figure 3–13 right shows the situation when the reference point does not lie on the rotation axis. Note that the coordinate differences  $\Delta\lambda_1$  (left) is not equal to  $\Delta\lambda_2$  (right). Consequently,  $\Delta\varphi_1$  is not equal to  $\Delta\varphi_2$ . Hence if compared to reference coordinates,  $P_1$  and  $P_2$  will show different patterns when rotating the UAS, even though they are in one and the same location with respect to the platform. This becomes especially important when determining the exact sensor offsets.

The differences of the AIProFlight-calculated sensor positions (using PP-coordinates) to the RTS coordinates are depicted in figure 3–14. Note that the differences are depicted with respect to the orientation of the UAS. Here, the sensor offsets were locally measured with respect to the given reference point using a sliding calliper, and entered to AIProFlight as specified in the manual (see figure 3–11).

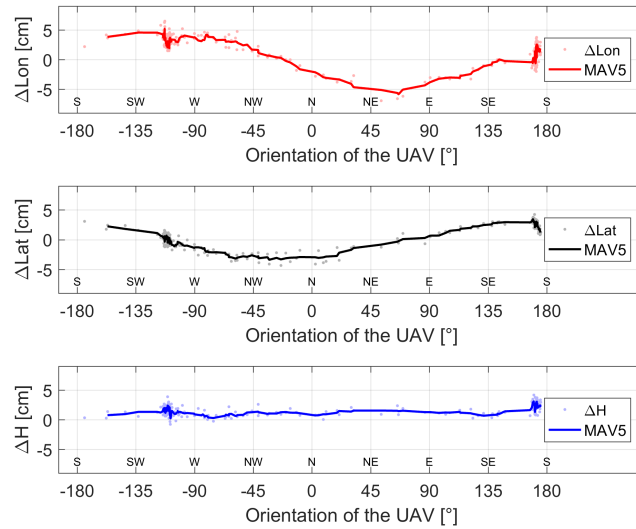


**Figure 3–14:** Differences to the reference sensor position, of the sensor position calculated from the PP-GNSS coordinates by AIProFlight using the sensor offsets from figure 3–11. Difference in longitude in red at the top, difference in latitude in black in the middle, and difference in height in blue at the bottom.

The orientation is measured magnetically, therefore the value 0 corresponds to magnetic north. The offset in the height component is constant, while the offsets in longitude and latitude resemble trigonometric functions. This indicates errors in at least two components of the sensor offsets.

#### Determination of the direction of the sensor offset axis

The results of earlier experiments suggested, that the actual direction of the sensor offset axis used in AIProFlights calculations does not coincide with the specified direction of the sensor offsets. This was tested by applying a large value (i.e. 50 cm) to one of the three sensor offset components while the other two remain 0. Figure 3–15 shows the results of this test.

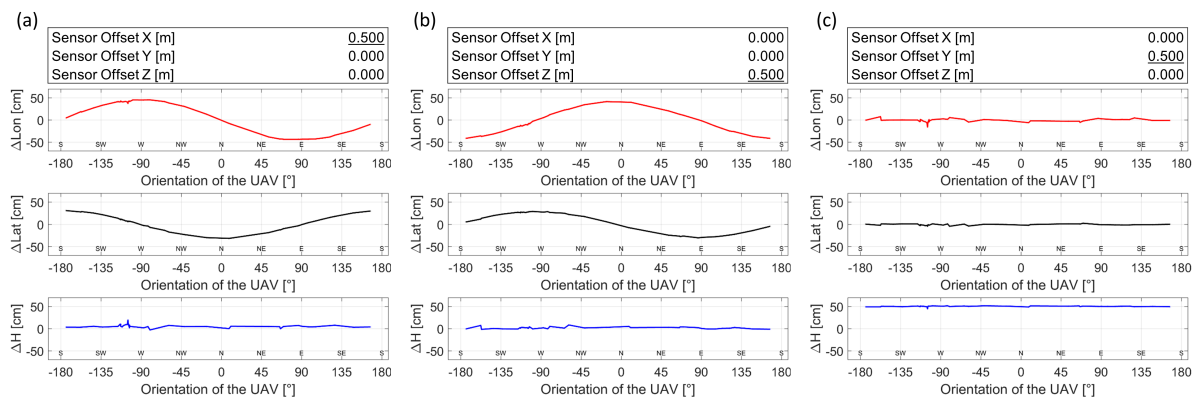


**Figure 3–15:** Coordinate differences to RTS measurements: (a), with x offset set to 50 cm, (b), with z offset set to 50 cm and (c), with y offset set to 50 cm.

### 3. ACCURACY INVESTIGATION OF THE UAS TRAJECTORY

From this test, the actual direction of the sensor offset axes can be determined. This is achieved by comparing the expected influence of one sensor offset axis on the coordinate axes ( $\lambda, \varphi, H$ ) to the actual influence of that sensor offset axis on the coordinate axes.

Sensor offset  $y$  is expected to largely influence the longitude when the UAS faces west, while largely influencing the latitude when the UAS faces north. In fact however, the sensor offset  $y$  is orientation independent and only influences the height component (see figure 3–15 (c)).

In the same manner, sensor offset  $x$  is expected to largely influence the latitude when the UAS faces west, while largely influencing the longitude when the UAS faces north. As can be seen in figure 3–15 (a), the coordinate differences actually show the expected influence of sensor offset  $y$  described in the previous paragraph.

Sensor offset  $z$  is expected to influence solely the height component, without depending on the orientation of the UAS. Actually though, the influence behaves as described to be expected from sensor offset  $x$  (see figure 3–15 (b)).

The observations described above, allowed us to conclude the actual directions of the sensor offset axes. Figure 3–16 shows the directions of the sensor offsets, once as specified by AIBotix, and once as determined above.

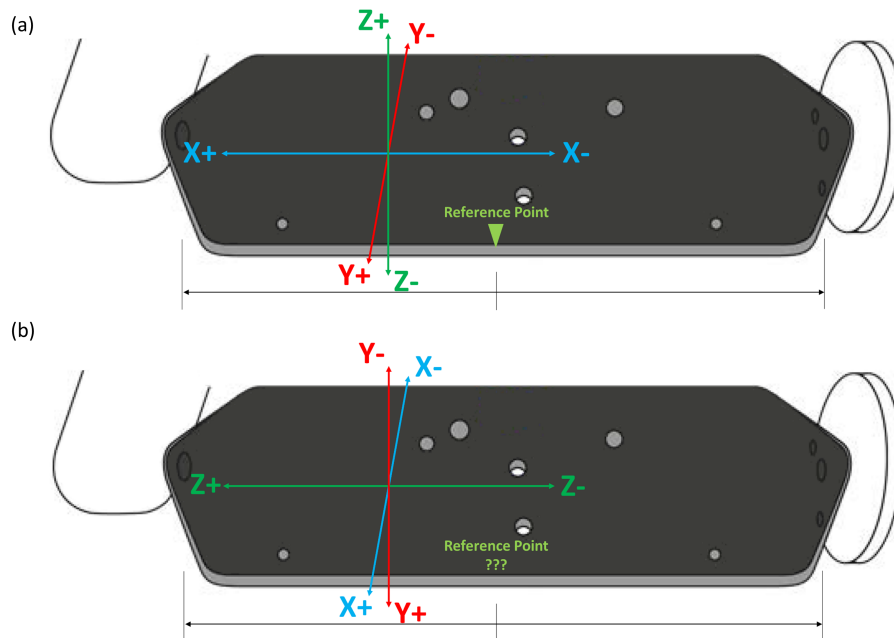


**Figure 3–16:** Directions of sensor offset components: a) as specified by AIBotix [3] (p. 45), and b) as taken from the test results in figure 3–15.

When entering the measured sensor offsets according to the newly found directions (figure 3–16 (b)), the orientation dependent difference gets smaller, yet it does not fully cancel out. This leads to the assumption, that the reference point does not coincide with the given reference point in figure 3–16 (a).

### Determination of the reference point and the correct sensor offsets

As the actual point to which the sensor offsets refer is unknown, the values of the offsets cannot be measured directly. Rather, they have to be determined from the data obtained in the experiment described in section 3.3.2. When entering 0 for all sensor offsets, the resulting trajectory describes the actual reference point. From its coordinate difference to the reference coordinates (measured by the RTS) of the prism, the actual sensor offsets can be deduced. Figure 3–17 shows the differences of the prism coordinates to the resulting trajectory when using 0 for all sensor offsets.

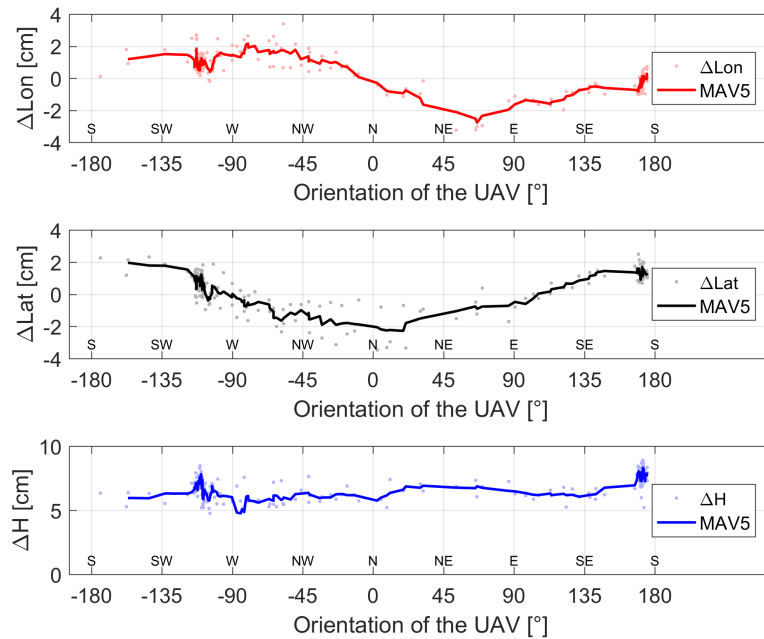


**Figure 3–17:** Differences of the prism coordinates calculated from the GNSS measurements by AIProFlight, to the prism coordinates measured by the RTS. Sensor offsets: [0 0 0]

The differences at different orientations of the UAS resemble harmonic oscillations in the longitude and latitude component, and a constant offset in the height component. The sensor offset which influences the height component (i.e.  $y$ , see 3–16 (b)) is simply the negative mean value of the differences in the height component.

The differences at specific orientations of the UAS would describe the other two sensor offsets  $x$  and  $z$ , however this only holds true if the reference point lies on the yaw-rotation axis of the UAS (see 3–13). Figure 3–18 shows the theoretical effect in the longitude component which the sensor offsets  $x$  and  $z$  would have in different orientations of the UAS. Note, that the the effect would also show in the latitude component, only it would be shifted by  $\frac{\pi}{2}$ .

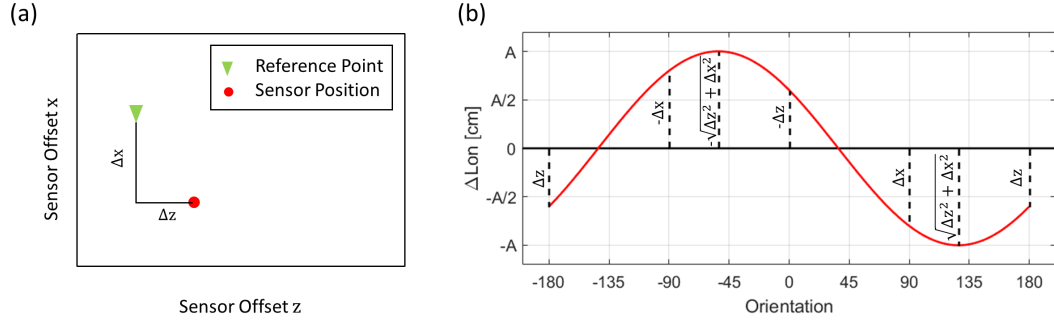


**Figure 3–18:** Sensor offsets  $x$  and  $z$ : (a) on the platform facing north, and (b) effect of different orientations of the UAS on the longitude difference between the reference point and the sensor position.

The sensor offset  $x$  could be read from the difference in longitude at 90 degrees, i.e. the UAS facing east. Accordingly, the sensor offset  $z$  could be read from the difference in longitude at 180 degrees, i.e. the UAS facing south. When applying this theory, the amplitude of the harmonic oscillation in the longitude and latitude differences decreases, but does not completely vanish. Consequently, the reference point does not lie on the yaw-rotation axis of the UAS (see figure 3–13).

The sensor offsets were therefore determined in an iterative way, by slightly altering the sensor offsets until the oscillation disappears in the coordinate differences. The so determined values for the sensor offsets  $x$ ,  $y$ , and  $z$ , as well as the originally measured sensor offsets with respect to the Given General Reference Point (GGRP) are presented in table 3–2. Note that the values given here refer to the newly found sensor offset directions specified in figure 3–16 (b).

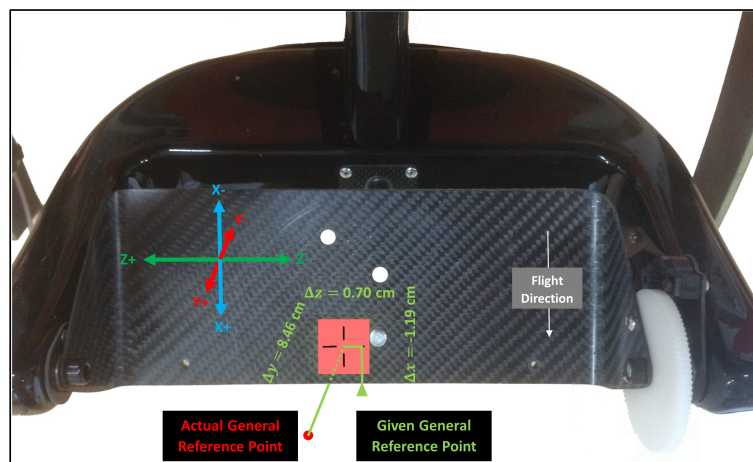
**Table 3–2:** Values of the sensor offsets in the directions determined in figure 3–16, measured to the GGRP, and determined iteratively based on the results in figure 3–17.

sensor offset	measured to GGRP [cm]	determined iteratively [cm]
$x$	-5.39	-4.20
$y$	2.06	-6.40
$z$	1.20	0.50

The differences between the sensor offsets with respect to the GGRP (table 3–2, column 2) and the sensor offsets determined from the experiment (table 3–2, column 1) yield the coordinates of the actual general reference point (AGRP) with respect to the GGRP. Hence, the sensor offsets referring to the AGRP for any payload, can be determined from the measured sensor offsets with respect to the GGRP after (3–9).

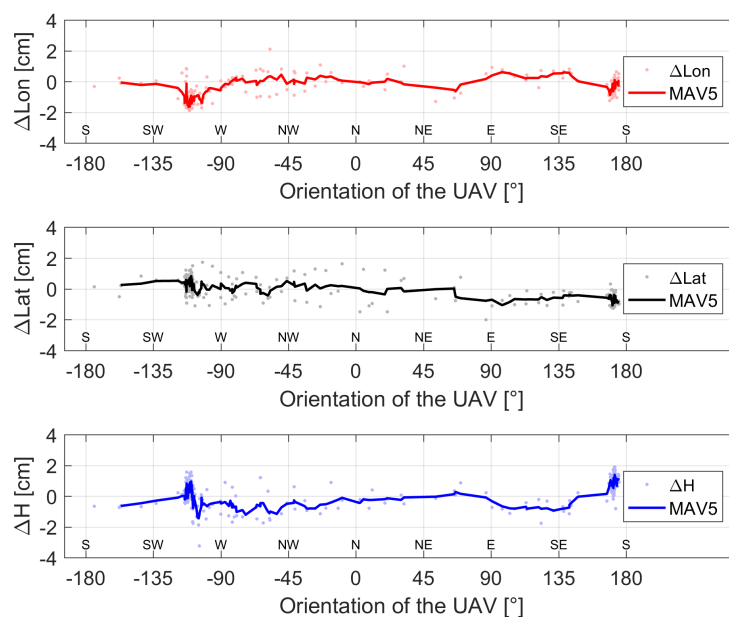
$$\begin{bmatrix} \Delta x \\ \Delta y \\ \Delta z \end{bmatrix}^{(\text{AGRP})} = \begin{bmatrix} \Delta x \\ \Delta y \\ \Delta z \end{bmatrix}^{(\text{GGRP})} + \begin{bmatrix} 1.19 \\ -8.46 \\ -0.70 \end{bmatrix} \text{ [cm]} \quad (3-9)$$

Figure 3–19 graphically shows the AGRP in relation to the GGRP.



**Figure 3–19:** Coordinates of the actual general reference point (red circle), relative to the given general reference point (tip of the green triangle).

Note that the AGRP is 8.46 cm below the platform! Using the sensor offsets with respect to the AGRP to transform to the sensor position, yields orientation independent coordinate differences, as seen in figure 3–20.



**Figure 3–20:** Differences of the prism coordinates calculated from the GNSS measurements by AIProFlight, to the prism coordinates measured by the RTS. Sensor offsets:  $[-4.20 \ -6.40 \ 0.50]^T$  [cm]

The remaining differences between the GNSS trajectory and the RTS trajectory are distributed around 0. The range of the differences is within the expected accuracy of relative GNSS processing techniques, i.e.  $< 5$  cm. Therefore, the remaining differences are not further investigated, and the here found Actual General Reference Point (see (3–9)) as

well as the new directions of the sensor offset components (see figure 3–16 (b)) are used for geotagging in all further experiments.

### 3.4 Results

Apart from the experiments used for the determination of the correct sensor offsets, we investigated the sensor position in two other scenarios. In the first scenario, we tried to establish ideal conditions for the GNSS measurements. This should give us an idea about the maximum reachable accuracy of the sensor position. In the second scenario, we simulated problematic conditions, i.e. the GNSS signal was partially obstructed. Figure 3–21 shows the trajectories as well as pictures of the two scenarios.

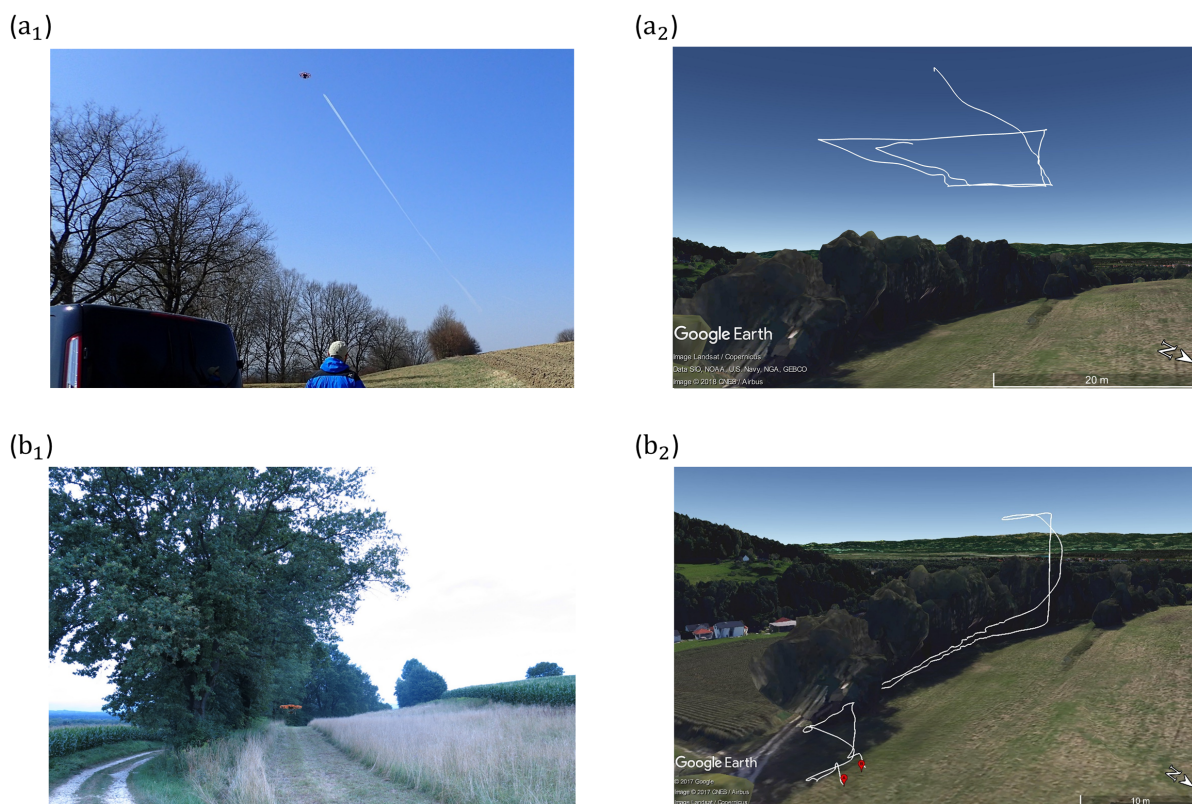


**Figure 3–21:** Impressions of the experiments under different GNSS conditions: a photograph and the trajectory of an experiment under ideal measurement conditions (a<sub>1</sub> and a<sub>2</sub>) and a photograph and the trajectory of an experiment under problematic measurement conditions (b<sub>1</sub> and b<sub>2</sub>)

During the first experiment, the flight height of the UAS exceeded the height of the obstacles, i.e. the trees. During the second experiment, the UAS actually flew beneath the branches and leaves of the trees (see figure 3–21, b<sub>1</sub>). We also tried to establish good conditions at one point in this experiment, when we increased the flight height on the west end of the trajectory (see figure 3–21, b<sub>2</sub>)

#### 3.4.1 Ideal conditions - no obstruction of the GNSS signals

As the flight height of the UAS exceeds the height of the trees, the GNSS reception is expected to be excellent, therefore also the quality of the solution should be excellent.

### 3. ACCURACY INVESTIGATION OF THE UAS TRAJECTORY

To quantify the quality of the PP-GNSS solution, the quality categories from NovAtels Inertial Explorer are used. This software was used to process the trajectory. NovAtel specifies the quality parameter as follows in their manual [17] (p. 37):

**Table 3–3:** Definition of quality categories by NovAtel.

Quality number	Description
Q1	fixed integer solution with good sat. geometry
Q2 & Q3	fixed integer solution with maginal geometry, or converging float solutions
Q4 & Q5	qualities similar to DGPS
Q6	C/A solution only

Note that this quality parameters only apply to the PP-trajectory. When using the OTF-solution of the UAS as basis for geotagging, no quality information is available.

#### Results from the PP-trajectory

The processed trajectory of the UAS, its quality (relating to table 3–3), as well as the differences to the reference trajectory are presented in figure 3–22.

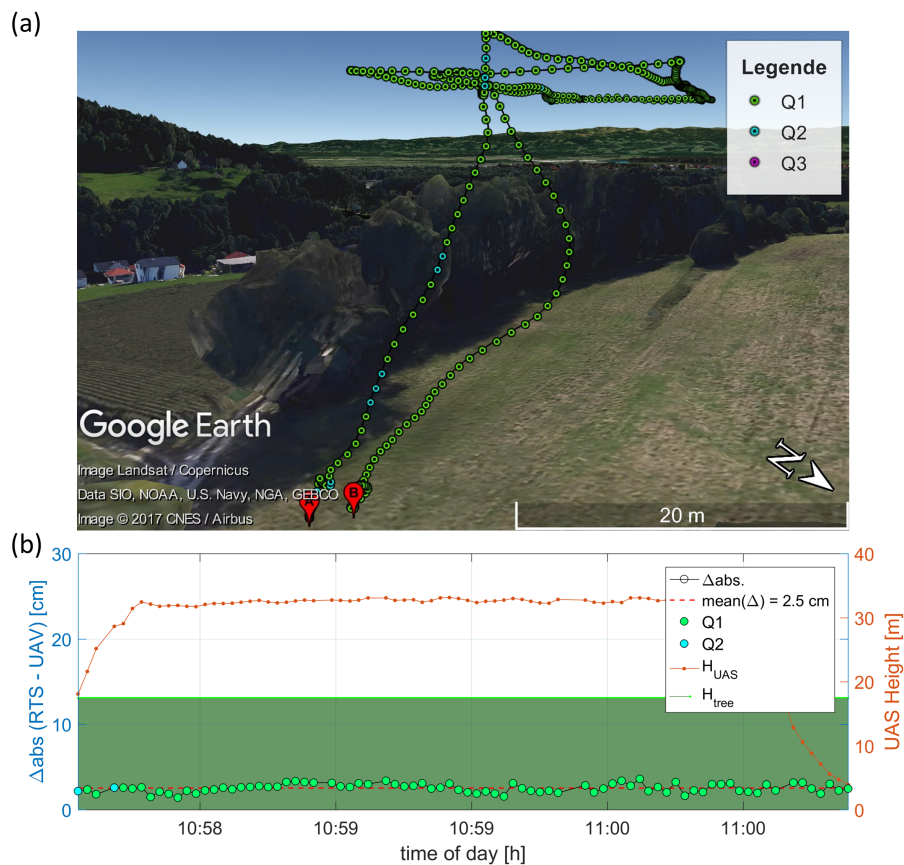


**Figure 3–22:** Ideal GNSS conditions, PP-approach: a) quality of the GNSS solution (see table 3–3), and b) difference to the reference trajectory with obstacle height (trees), flight height of the UAS and GNSS quality of the used point.

In figure 3–22 (a), point A represents the start point and point B represents the landing point. The points in between are the GNSS solutions processed with Inertial Explorer, where the colour of the points represents the quality of the respective point. The position solution is available with a frequency of 20 Hz, for better clarity however, only every 10th point is depicted here. Note that the camera took pictures (created events) at a frequency of 0.5 Hz, thus creating GNSS-based coordinates of  $P_{\text{Sens}}$  at 0.5 Hz. Figure 3–22 (b) shows the absolute differences between  $P_{\text{Sens}}$  measured by the RTS and  $P_{\text{Sens}}$  measured by GNSS. Every difference is also coloured according to the quality of the PP-GNSS solution used in the difference. The brown line represents the flight height of the UAS over time, while the green belt represents the height of the line of trees south of the trajectory (see also figure 3–22 (a)).

Apart from two points in the beginning, the quality parameter of the points used in the difference is always Q1, which represents the highest quality (see table 3–3). In addition, the ambiguity fix was never lost during the flight. Note, that figure 3–22 stands exemplary for a total of four flights with comparable, ideal conditions. Graphical results from the other flights are presented in appendix A. Numerical results are presented in table 3–4.

**Table 3–4:** Expected absolute 3d-difference in ideal GNSS conditions

Flight Nr.	Date	mean( $\Delta$ ) $\pm$ 1 $\sigma$ [cm]	95th percentile [cm]	normally distributed ( $\alpha = 5\%$ )
0005	2017/03/16	2.3 $\pm$ 0.7	3.2	✓
0007	2017/03/16	1.7 $\pm$ 0.8 <sup>1</sup>	3.3	✗
0019	2017/07/20	2.5 $\pm$ 0.5	3.3	✓
0020	2017/07/20	1.9 $\pm$ 0.4	2.5	✓
Total		2.2 $\pm$ 0.6	3.2	✓

The values presented here are the mean absolute point differences i.e. the expected direction-independent difference from the reference trajectory for every event. A Kolmogorow-Smirnow-Test [19](p. 427) showed that the differences from every separate flight (except for flight 0007), as well as the total set of differences from all flights follow a normal distribution ( $\alpha = 5\%$ ). For a visual check, the cumulative frequency, the histogram and the qq-plot of the total set of all differences are presented in figure 3–23.

---

<sup>1</sup>During this flight, the trigger frequency of the camera was set to be 1 Hz. This high frequency led to systematic differences. Also, the manufacturer warned of "strange-platform behaviour" at frequencies higher than 0.8 Hz. Therefore the differences from this flight are excluded from the total mean difference.

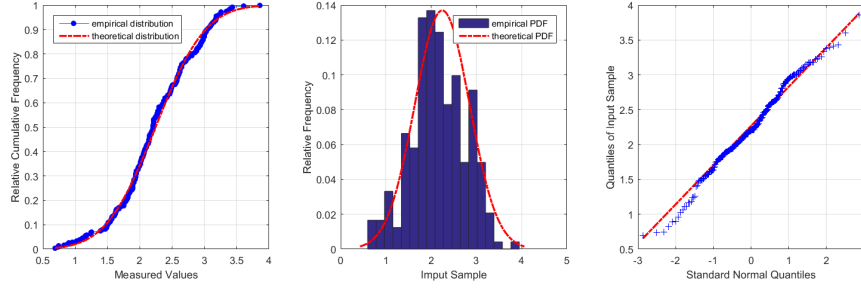


**Figure 3–23:** Cumulative frequency-, histogram- and qq-plot of the absolute differences at ideal GNSS conditions (from right to left).

For all events, the expected absolute difference amounts to 2.2 cm with 95 % of the differences being smaller than 3.2 cm. This expected difference does not only apply to the prism, but also to any other point on the platform, e.g. a camera. Using camera positions of this quality for georeferencing will influence the ground point accuracy. The ground point accuracy of this approach compared to the conventional approach (i.e. using GCPs) is investigated in section 4.

### Results from the OTF-trajectory

In the same manner as in the previous section, the test trajectory (i.e. the OTF-trajectory) is compared to the reference trajectory at the times of the events. The differences in the single coordinate components for all experiments<sup>2</sup> with ideal GNSS conditions are presented in figure 3–24. For comparison, not only the differences of the OTF-solution, but also the differences of the PP-solution (discussed in the previous section) are depicted.

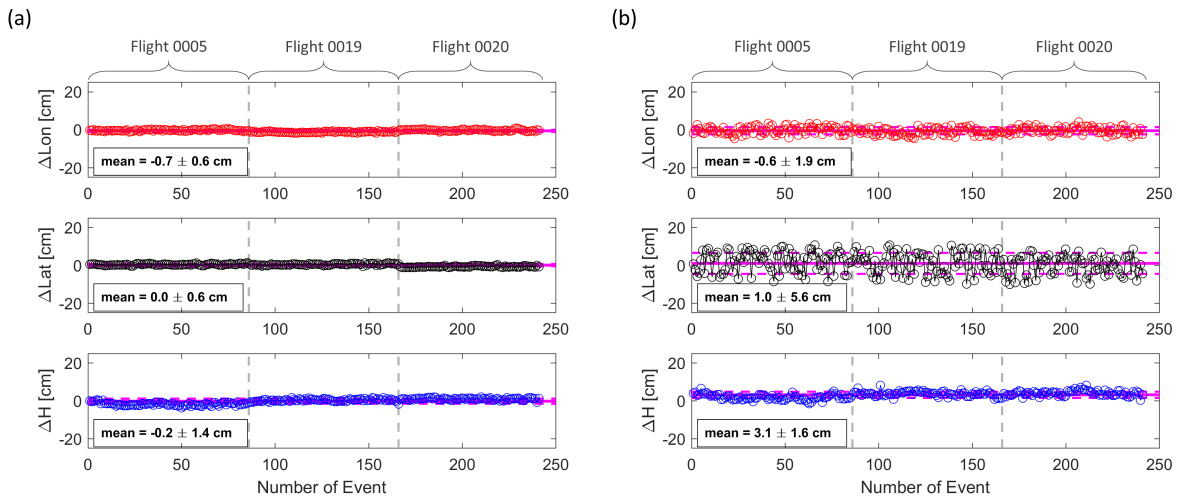


**Figure 3–24:** Ideal GNSS conditions (flights 0005, 0019 and 0020): difference to reference trajectory in all three coordinate directions (longitude, latitude and height), a) of PP-solution, and b) of OTF-solution.

The differences from the OTF-solution in figure 3–24 (b), show a considerably larger variance than the differences from the PP-solution in figure 3–24 (a). Especially in the

<sup>2</sup>Flight 0007 is again excluded here, due to the high trigger frequency and the problems involved (see also section 3.4.1).

latitude component, an increase by almost a factor 10 is visible! This is orientation-independent, as the large variance appears both in flights 0005 and 0019 (UAS faced west) as well as in flight 0020 (UAS faced south). Part of this effect could be the result of the different processing methods. While the PP-trajectory can be calculated as a combination of processing in forward and reverse time, the OTF-trajectory can be calculated from the forward time solution only. The effects of combining forward- and reverse time processing are discussed by Hutton [12]. The OTF-processing takes place entirely inside the NovAtel unit onboard of the UAS. Hence, besides the coordinates at the events, no information whatsoever is visible to the user. Therefore, the increased variance in the latitude component when using the OTF-workflow could not be investigated any further.

The absolute direction independent differences to the reference trajectory of the OTF-solution as well as the PP-solution are depicted in figure 3–25.

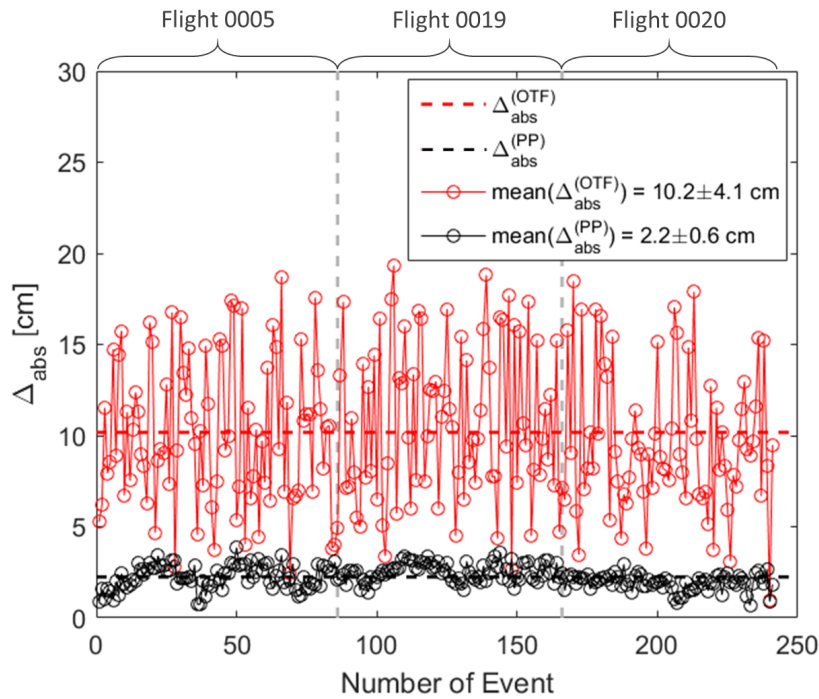


**Figure 3–25:** Ideal GNSS conditions (flights 0005, 0019 and 0020): absolute difference to reference trajectory of PP-solution (black), and of OTF-solution (red).

The OTF-coordinate differences depicted in figure 3–24 (b) result in an absolute direction-independent difference of  $10.2 \pm 4.1 \text{ cm}$ . This equals more than 4 times the difference from the PP-trajectory! Therefore, the PP-solution, rather than the OTF-solution will be used for directly georeferencing the pictures without ground control points in section 4.

#### 3.4.2 Problematic conditions - partial obstruction of the GNSS signal

As described above, problematic conditions are established by flying beneath the branches and leaves of a line of trees. Two flights were carried out for this scenario, one in March (no leaves on the trees) and one in July (leaves on the trees). Figure 3–26 shows the line of trees at the different points in time.



**Figure 3–26:** Obstructive line of trees in different states: (a) during the flight in March, and (b) during the flight in July.

It is expected, that the trees without the leaves will be less obstructive to the GNSS signals than the trees with the leaves. Figure 3–27 shows the absolute point differences of the flight carried out in March.

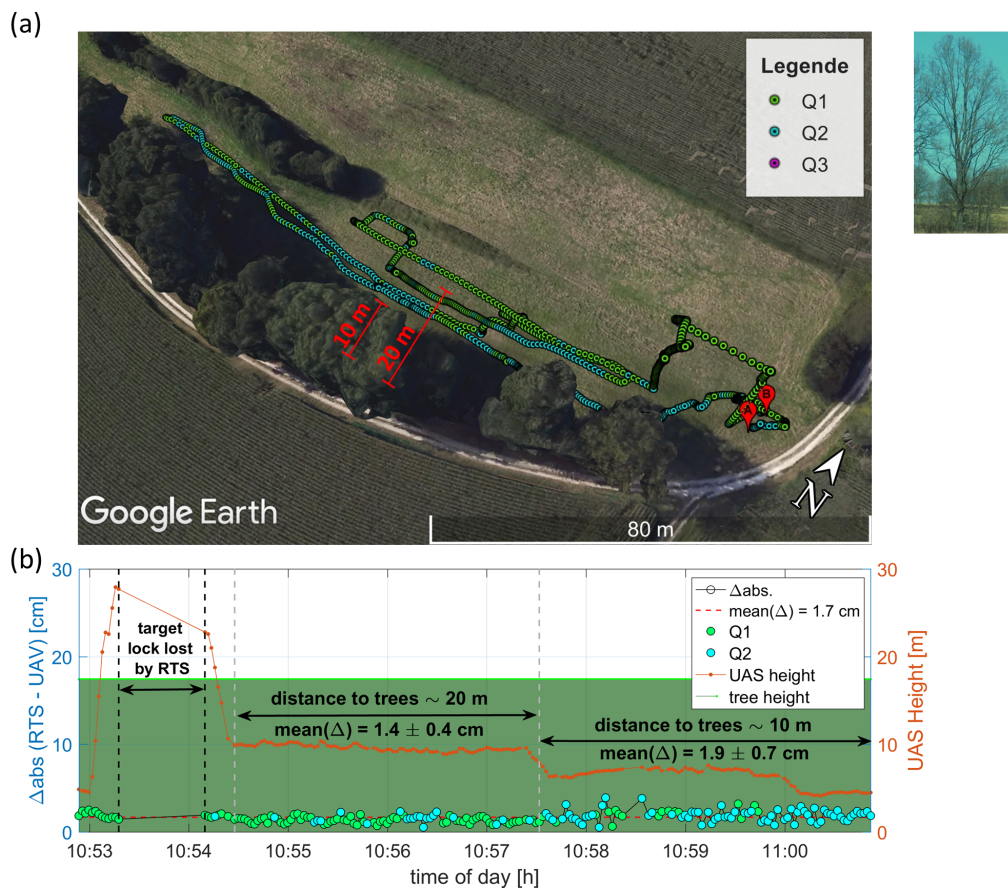


**Figure 3–27:** Problematic GNSS conditions (no leaves on trees): a) quality of the GNSS solution (see table 3–3), and b) difference to the reference trajectory with obstacle height (trees) and flight height of the UAS.

During this flight the UAS flew in different distances to the line of trees. At the beginning of the flight, the UAS flew above the trees, thus without obstruction from the tree line at all. During this time however, the RTS lost track of the target for 52 seconds due to a fitful movement of the UAS. For that reason, there is little data available during this time. The available data shows excellent GNSS quality (Q1) for all but one point. Then the UAS height decreased below the level of the tree height while staying about 20 m away from the tree line. During this time, several points of quality Q2 also occur in the data. The mean value of the absolute point difference during this time amounts to 1.4 cm. After the flight with 20 m distance to the line of trees, the UAS flew with about 10 m distance to the line of trees. This leads to stronger obstruction and therefore to a rise of the mean value of the differences as well as their standard deviation from 1.4 to 1.9 cm and from 0.4 to 0.7 cm respectively. Also the quality parameter is mostly Q2 during this time. For the entire dataset, the differences are not normally distributed ( $\alpha = 5\%$ ). Nevertheless, the ambiguity fix was never lost, and all differences are within the expected value of 2.1 cm for unobstructed flight (see section 3.4.1). Hence in this case, vegetation without any leaves (during the winter month) does not obstruct signals from GNSS satellites in a way, that largely influences the accuracy of the GNSS solution. The influence on the accuracy of the UAS trajectory in any given situation however largely depends on the kind of obstruction, the relative position of the GNSS antenna to the obstacle, as well as the satellite constellation. Therefore, this results are not universally valid and would

need to be repeated in other scenarios to assess the actual influence on the accuracy of the UAS trajectory.

For the second flight in July, the leaves had already grown, establishing a more severe obstruction for the GNSS signals. The trajectory as well as the differences to the reference trajectory are depicted in figure 3–28.

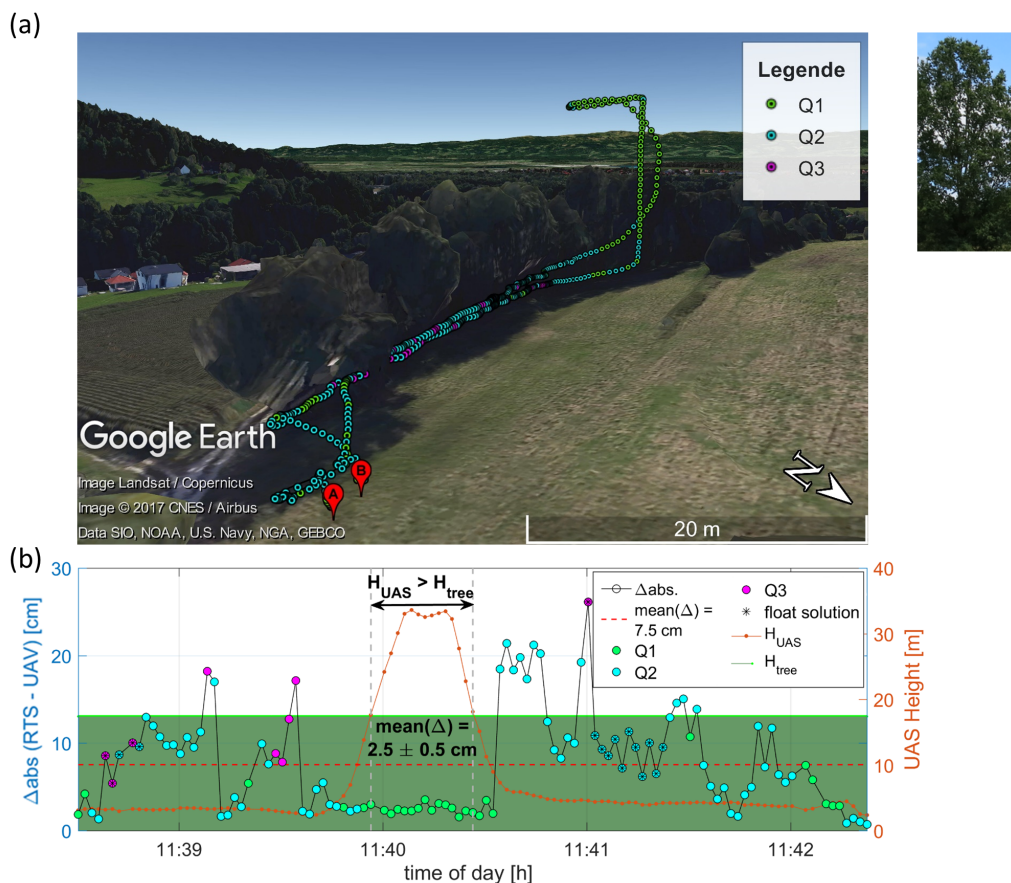


**Figure 3–28:** Problematic GNSS conditions (leaves on trees): a) quality of the GNSS solution (see table 3–3), and b) difference to the reference trajectory with obstacle height (trees) and flight height of the UAS.

The flight took place almost entirely under the trees. At the western end of the trajectory, the UAS rose above the tree line for a short period of time. During that time, the quality parameter could reach Q1. In this period, the differences follow a normal distribution ( $\alpha = 5 \%$ ) and the mean value of the differences sinks from around 9 cm to 2.5 cm.

The sections of the trajectory before and after the height increase show different behaviour. The differences are not normally distributed ( $\alpha = 5 \%$ ) and show jumps of up to 16 cm from one event to the next ( $\Delta t = 2 \text{ s}$ ). In addition, the ambiguity fix is lost twice during the flight. To tackle this problem, one might think of only choosing solutions of the highest quality (Q1) for georeferencing. This would however result in large data gaps and consequently most picture positions could not be used. Also, Q1 quality does not necessarily mean high accuracy as evident in figure 3–28 (b). One event of quality Q1 even has an error of almost 11 cm. Using the OTF solution, filtering according to

### 3. ACCURACY INVESTIGATION OF THE UAS TRAJECTORY

the quality of the solution is not possible, because no quality information is available for this solutions. To gain a better understanding for the differences from figure 3–28 (b), figure 3–29 shows the skyplot, as well as the signal to noise ratio (SNR) of selected GPS satellites.

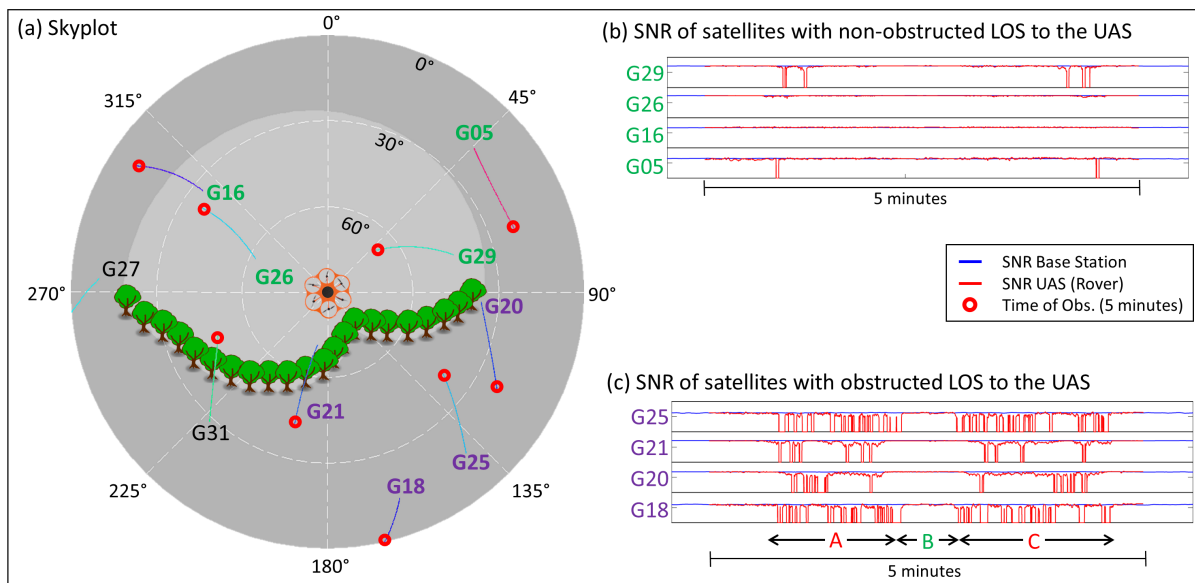


**Figure 3–29:** Flight ID 0023 (partly obstructed GNSS signal): a) Skyplot during the measurement situation, b) SNR values for satellites north of the obstructive line of trees and c) SNR values for satellites south of the obstructive line of trees.

The skyplot shows the satellite constellation during the flight. Please note, that the one-hour satellite tracks are depicted in figure 3–29 (a), while the flight itself only lasted five minutes. This measurement time is indicated at the beginning of each satellite track by a red circle. The same period of time is depicted in figure 3–29 (b) and (c) where the blue line represents the SNR of the base station, and the red line represents the SNR of the rover, i.e. the UAS. The SNR of the UAS in both, figure 3–29 (b) and (c) are roughly mirrored with respect to the middle section (B). Considering, that the UAS flew first in direction west, then rose above the trees, and then went back east the same way it came, this behaviour is expected.

Figure 3–29 (b) shows the SNR values of the satellites north of the line of trees. Therefore, no signal obstruction is expected for this satellites. However, the signals of G29 and G05 show a drop of the SNR value to zero for a few seconds. This indicates a total loss of the signal. Note that both satellites are roughly in the same direction with respect to the UAS during the measurement (see figure 3–29 (a)). In addition, the signal loss occurs on both, the way to the western end of the trajectory and the way back to the starting point. These two factors indicate an obstacle in direction of the satellites. As the signal loss is of such short duration and only occurs twice in G29 (one way) and once in G05, the obstacle must be rather small.

Figure 3–29 (c) shows the SNR values of the satellites south of the line of trees. The SNR values in section A and C indicate multiple signal losses and regains of the signal at a high frequency. Figure 3–30 shows the SNR of satellite G25 in more detail, together with the flight height of the UAS, and the height of the obstacle, i.e. the line of trees.

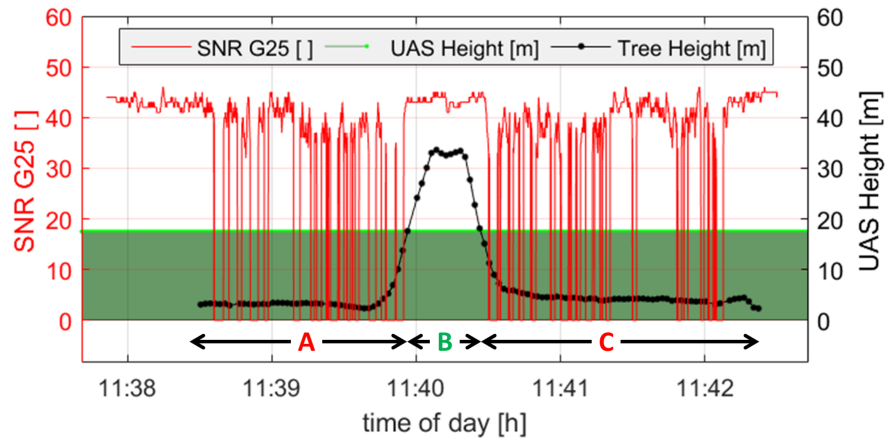


**Figure 3–30:** SNR value of satellite G25 (red) and flight height of the UAS (black).

After about 2 minutes of flight time, the SNR value of all satellites stabilises (section B). During this time, the UAS rose above the line of trees thus the signal did not experience any obstruction there. When lowering the UAS height back under the line of trees (section C), the SNR values again show a high frequented loss and regain of the satellite signals. This signal losses in section A and B change the geometry of the measurement situation rapidly thus causing large jumps in the absolute position of the UAS (see figure 3–28 (b)).

## 4. Accuracy investigation of points, measured from the UAS

In section 3.4.1 it was shown, that a sensor accuracy of 2.2 cm can be achieved when pursuing the post processing approach in non obstructed situations. It is expected, that employing picture positions of this accuracy as basis for georeferencing rather than GCPs will influence the accuracy of object points on the ground. The following experiment should show this influence and allow a statement about possible applications of this novel approach based on the found accuracy.

### 4.1 Measurement setup and processing approach

#### 4.1.1 Description of the flight area

The area in which the experiment could take place must meet certain criteria. The legal aspects of UAS based surveying must be taken into consideration and are roughly described in section 2.4. With a category A admission, which the Institute of Applied Geosciences holds, almost the entire area of Graz is disqualified as possible flight area for this experiment. Therefore, an area about 20 km South of Graz was chosen for the test flight. Figure 4–1 shows an overview of the flight area.



**Figure 4–1:** Flight area in Mellach.

The area within the red boundary indicates the flight area. This area includes a gravel path on the right side, as well as a line of trees at the top and a field in the center. In addition to that, we flew over the white house within the red boundaries. This is the private house of our drone pilot, who agreed to cover it with the UAS, and to grant us access for terrestrial reference measurements. As opposed to GCPs, Points around the house and garden represent points, that are actually surveyed in reality. Hence, their accuracy is more representative for actual surveying applications.

### 4.1.2 Description of the points of interest

For this experiment, a routine image flight over a specified area (see section 4.1.1) was undertaken with the UAS. A total of 61 points of interest (POIs) were chosen in this area. All of them were measured photogrammetrically as well as by means of conventional surveying using an RTS and a round prism on a pole. The local point coordinates measured by the RTS were transformed to WGS84 in the same way as in previous experiments concerning the sensor accuracy (see section 3.3.1). These global coordinates (measured by the RTS) serve as reference coordinates for future comparisons.

The 61 POIs consist of 15 GCPs, 17 colour markers and 29 object points. The GCPs were distributed throughout the whole flight area while the object points were set only around the detached house. This is because nowhere else in the scene, naturally recognisable points appear. Colour markers on the gravel path should nevertheless allow points being measured on natural underground (i.e. gravel) instead of the smooth surface exhibited by the GCPs or the object points. Figure 4–2 shows examples from each of these three point groups.

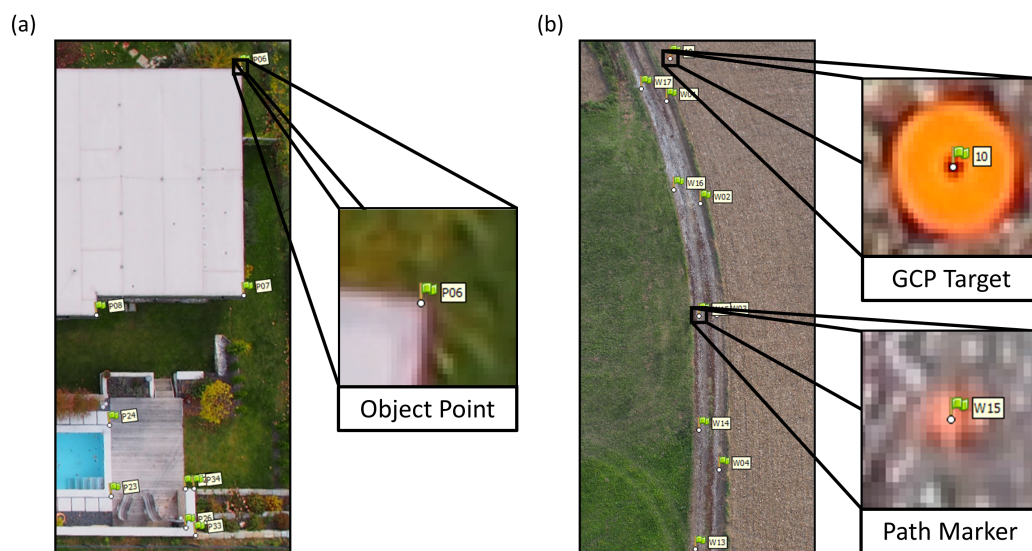


**Figure 4–2:** Examples for POIs as seen in the taken pictures, (a) object points (no artificial marker), and (b) GCP target on the top, and color marker on the bottom.

Object points have to be distinctly recognisable in both, the pictures and in nature (for RTS reference measurements). Points with this property are for example corners of walls, rooftops or other structures. Nevertheless, object points are more difficult to measure than GCP targets or colour markers. This becomes visible when comparing figure 4–2 (a) to figure 4–2 (b). The corner of the roof is more difficult to be exactly identified in the picture, than the centre of the GCP target or the colour marker. The same is true for the reference measurements by the RTS. This results in a lower accuracy of object points to begin with. In real world applications however, it is more common to determine object points, rather than GCPs or colour markers.

### 4.1.3 Processing approach

For the calculation of point coordinates from the pictures, Agisoft Photoscan (PS) was used. Two different approaches were carried out and evaluated. First, object point coordinates were calculated using the conventional, GCP based approach. Then, the novel approach using solely the GNSS positions of the pictures was carried out. The workflow in Agisoft Photoscan is elucidated below.

#### Workflow in PS: conventional approach, using GCP based georeferencing

**Step 1:** After sorting through the taken pictures and eliminating the blurry or otherwise corrupted ones, the remaining pictures can be imported in Agisoft Photoscan.

**Step 2:** The image coordinates of all POIs should be measured in all (but at least in 2) pictures in which they are visible. This is done by simply clicking on the point in the picture causing a marker with a unique ID to be created. The ID can be used in other pictures as well, indicating to the software that the points are identical. Special attention should go to the measurement of the very GCPs, that will be used in georeferencing, i.e. aligning of the pictures. We used 4 GCPs in this experiment.

**Step 3:** Previously calculated, global coordinates of the GCPs are imported to Agisoft Photoscan. These coordinates were measured by means of relative GNSS.

**Step 4:** In this step the pictures are aligned, according to the global positions of the GCPs and identical points. The identical points are detected automatically in adjacent pictures. The user can decide how many points should be used for the alignment. We used the 400 statistically most accurate points out of 4000 automatically detected points for each pair of pictures.

**Step 5:** Once the pictures are aligned, a dense point cloud (DPC) can be calculated from them. This step takes by far the longest, as processing times of several hours are common. Also, the coordinates of the POIs are calculated. All of the data can be exported for further processing.

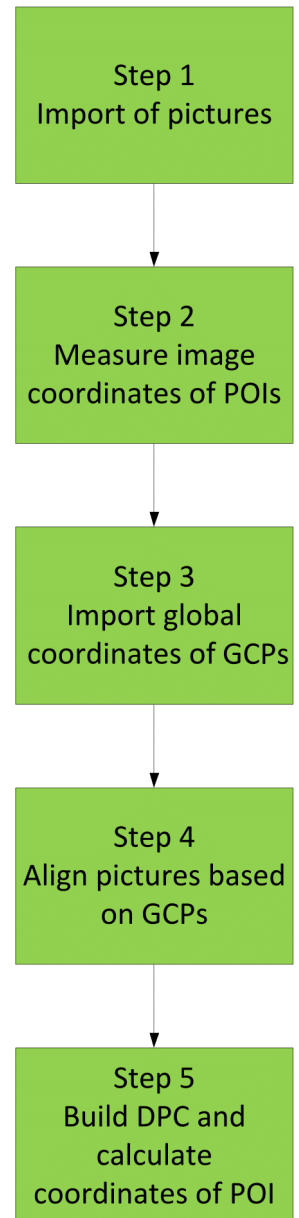


**Figure 4–3:** Workflow for the conventional, GCP based approach in Agisoft Photoscan.

### Workflow in PS: Novel approach, using GNSS based georeferencing

**Step 1:** While the import of the pictures stays the same as in the conventional workflow, the pictures themselves have been pre-processed. They are assigned a GNSS position by AIProFlights function GeoTagging (see section 2.2). The GNSS position is written directly to the picture, using the EXIF [4] (p. 13) format.

**Step 2:** The measurement of the image coordinates of the POIs is identical to the conventional workflow. Note however, that the measurement of the GCPs in this case is only done for evaluation purposes and would not be necessary in real applications.

**Step 3:** For more stability of the alignment result, known distances can be introduced in Agisoft Photoscan. In addition to known distances on the ground, the software also allows for distances between picture positions to be entered. These distances are calculated from the GNSS positions of the pictures. It is however not possible to import the distances from an ASCII file, hence they have to be entered manually. We used the 6 distances between the 4 pictures at the corners of the flight area (see figure 4-1).

**Step 4:** The alignment of the pictures is carried out, based on their GNSS positions, the known distances and identical points in adjacent pictures. As in the conventional approach, these are detected automatically.

**Step 5:** The calculation of the DPC and the POIs is identical to the conventional approach.

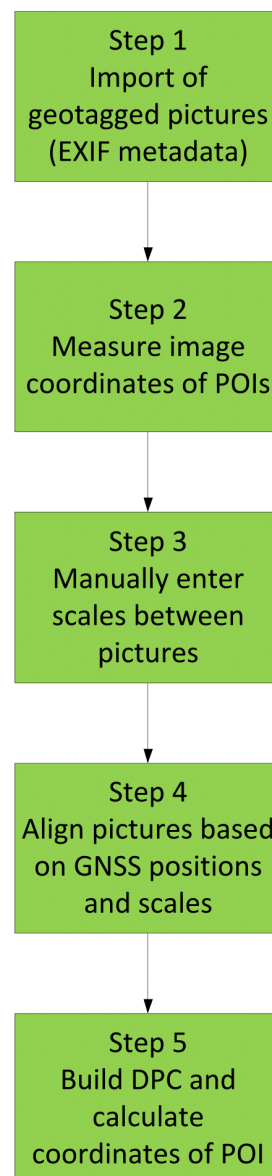


**Figure 4-4:** Workflow for the novel, GNSS based approach in Agisoft Photoscan.

## Point Cloud Comparison

When comparing point clouds to each other, some aspects have to be kept in mind. Rather than measuring specific targets, a raster of points is collected whose node locations will most certainly not be identical in both datasets. Hence, corresponding points in both point clouds are defined by mathematical models and do not necessarily represent actually identical points. In this way, small alignment errors between the point clouds directly influence the distance between corresponding points.

There are many different software solutions for point cloud comparison, however we used Cloud Compare for the comparisons presented in section 4.2.1. Cloud Compare offers different approaches on how to calculate the difference between two point clouds, two of which I want to elaborate on.

### Nearest Neighbour:

Nearest Neighbour is the most simple, and also default approach by Cloud Compare. For every point of the point cloud, a distance to the reference point cloud is calculated. This distance is simply the euclidean distance between the current point, and its closest point in the reference point cloud. Despite this being a very efficient method for calculating distances between point clouds, it can cause problems. Figure 4–5 shows a schematic representation of two point clouds.

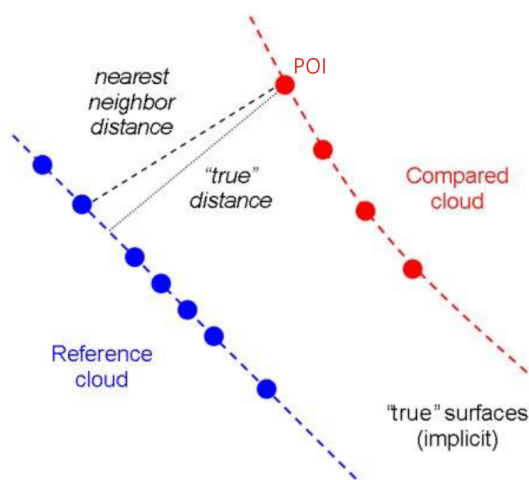


**Figure 4–5:** Schematic representation of a point cloud and the nearest neighbour distance of one of its points to a reference point cloud (Source: Cloud Compare manual [9] (p. 29)).

The blue points represent the reference point cloud while the red points represent the compared point cloud. Assume that the dashed blue and red lines actually are the true surfaces of the reference- and the compared cloud respectively. Then the true distance between the POI<sup>1</sup> and the surface is actually shorter than the nearest neighbour distance.

<sup>1</sup>Please note, that this POI does not refer to the POIs discussed in section 4.1.2. Here, POI simply indicates the current point which the distance refers to.

##### Least Squares Plane:

A slightly more sophisticated approach is implemented in the option "Least Squares Plane". In this approach, the nearest neighbour is not the only point that is included in the distance calculation between the point clouds. An optional number of points greater than 2 around the nearest neighbour can be used to locally estimate a plane surface in the reference point cloud. The distance of the POI to the reference point cloud is then defined as the shortest distance between the POI and the local plane. In the schematic example presented in figure 4–5, this distance would be much closer to the "true" distance than the Nearest Neighbour distance. This does however only hold true, if the reference point cloud does not exhibit high curvature. If this would be the case, the local model would have to be changed from a plane surface to e.g. triangulation or a surface of higher order.

Both described methods are of the family of Cloud-to-Cloud (C2C) comparisons. Further methods for point cloud comparison are Cloud-to-Mesh (C2M), Mesh-to-Mesh (M2M) and Multiscale-Model-to-Model-Cloud (M3C2) comparisons. C2M calculates the shortest distance of a POI to the nearest triangle of a mesh. M2M calculates the the shortest distance between two triangles of two meshed models. The normal vectors of both triangles are used to define the direction of the shortest distance. M3C2 is a method that is uniquely available in Cloud Compare. It takes the registration accuracy and the local variance around a POI into account when selecting a corresponding point in the second point cloud and calculating their distance to each other. This allows Cloud Compare, to determine which distances are significant. The significance however largely depends on the registration accuracy, which can be manually entered by the user and is thus not free from subjective influence. More on this algorithm can be taken from Lague et. al 2013 [13] and by Girardeau-Montaut 2015 [9] (p. 165-167).

Holst et. al concluded in 2017 [11], that C2C and C2M comparisons are not suitable if complex surfaces or inhomogeneous surface properties are exhibited by the compared point clouds. In addition, without prior knowledge about the object, the influence of actual deformation, registration errors, systematic errors, shadowing, surface properties and object properties on the C2C distance cannot be separated from each other.

However in the comparison conducted here most of this influences can be eliminated due to the special situation, that both point clouds come from one and the same dataset. The only difference between them is the georeferencing approach which is done once using GCPs, and once using GNSS positions of the pictures. Hence no actual deformation, shadowing, differing surface or object properties between the two point clouds are existent. Due to this special property of the point clouds and the relatively smooth surface, the "Least Squares Plane"-approach was used to calculate the distances between the point clouds.

## 4.2 Results

In step 5 of both processing approaches presented in the previous section, a DPC is calculated. After deleting trees, bushes and outliers from both point clouds, a comparison between them is carried out by means of local Least Squares Plane modelling (see section 4.1.3). In addition, the resulting coordinates of the POIs from both approaches will be compared to the reference coordinates, measured by the RTS. The reference coordinates are also used to compare 3d distances between POIs. This should grant insight into their relative accuracy. To assess the accuracy of values that are deduced from the DPC, the roof inclination of visible buildings will be calculated from both approaches and compared to each other.

### 4.2.1 Point Cloud Comparison

The point cloud comparison was carried out with the software Cloud Compare. Before comparing the two point clouds however, 3dReshaper was used to remove trees and bushes from both point clouds. This is done, because especially leaves move a lot in the wind, leading to different positions of one and the same leave in different pictures. Hence this points tend to be very noisy and therefore do not represent a realistic measurement situation, i.e. a stationary scene.

The remaining points are used to calculate the 3d distances between the two point clouds. Figure 4–6 shows the DPC from the novel approach, once in real colours and once coloured by distance from the reference point cloud, i.e. the DPC from the conventional approach.

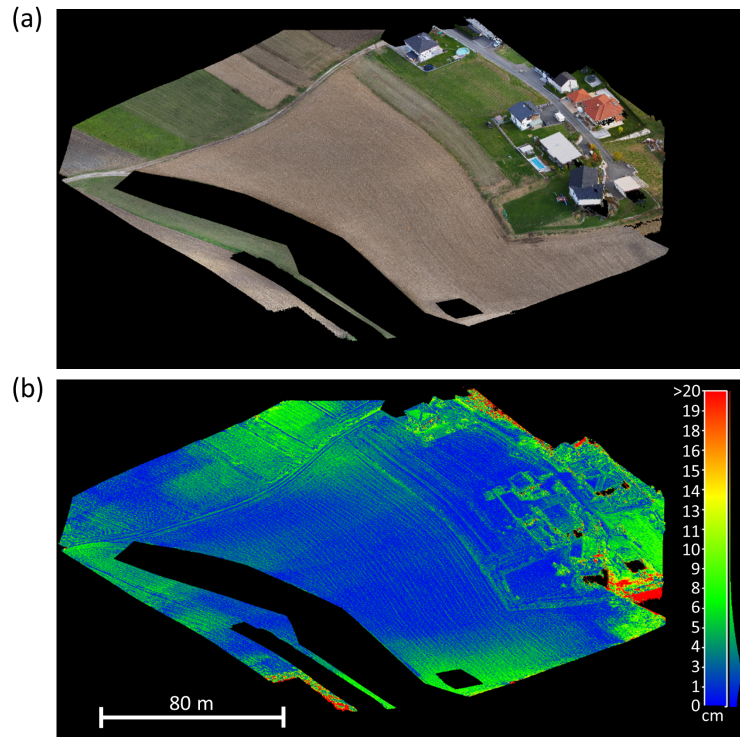


**Figure 4-6:** Calculated DPC: (a) DPC from novel approach in real colours, and (b) absolute distances (< 20 cm) of DPC from novel approach to DPC from conventional approach. The distances are calculated using local least square plane modelling.

The distances on the open field in the middle of the DCP as well as on the roofs of the buildings and the free parcel between the houses is around 3 cm. Boundaries between different types of underground show differences between 5 and 10 cm. This is evident at edges of building roofs, as well as at natural boundaries between fields of different coverage. At the edges of the point cloud, even larger differences can occur. These can be the result of insufficient overlapping of the point cloud or simply blunders in one point cloud or the other. Figure 4-7 shows a histogram of the differences shown in figure 4-6 (b).

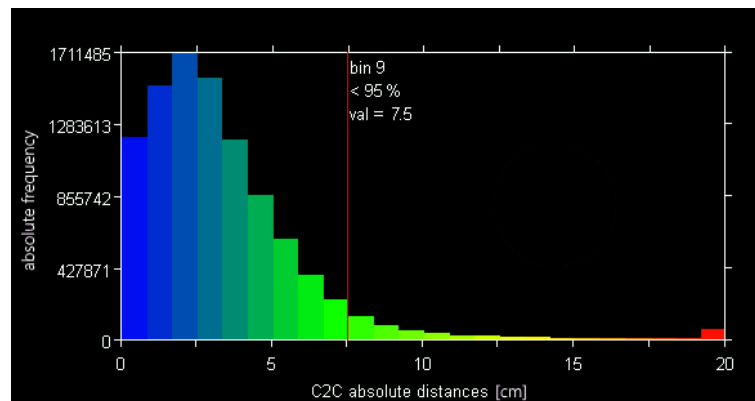


**Figure 4-7:** Absolute frequency of distances between DPC from conventional approach and DPC from novel approach. This histogram shows the original data, which is not cleaned from blunders yet.

Note that all differences larger than 20 cm are summarised in the last class (red). After eliminating blunders using robust median-absolute deviation [19] (p. 338), the mean value of the distances amounts to 2.9 cm, with 95 % of the differences being smaller than 6.5 cm. This suggests a high accuracy of results using the novel approach, please note however that we do not compare actually identical points here. Rather we compare the closest points, hence this distances do not necessarily show referencing errors such as small rotations or shifts of the point cloud. To assess possible referencing errors, the coordinates of the POIs (see section 4.1.2) are compared to each other.

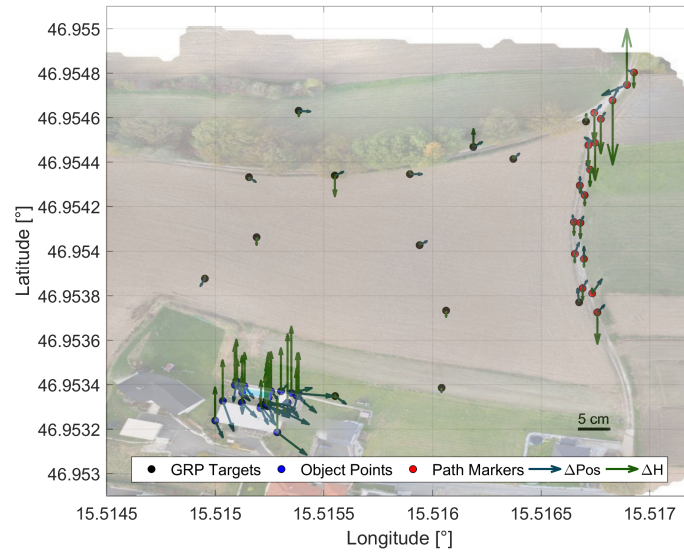
### 4.2.2 Accuracy of Single Point Positions

All POIs were measured photogrammetrically as well as by means of RTS. This allows for a direct comparison of the resulting coordinates. Note that the so found difference between the single points are mainly influenced by three components:

1. Errors from georeferencing
2. Errors from the measurement of the point in the pictures
3. Errors from the measurement of the point in the field using RTS

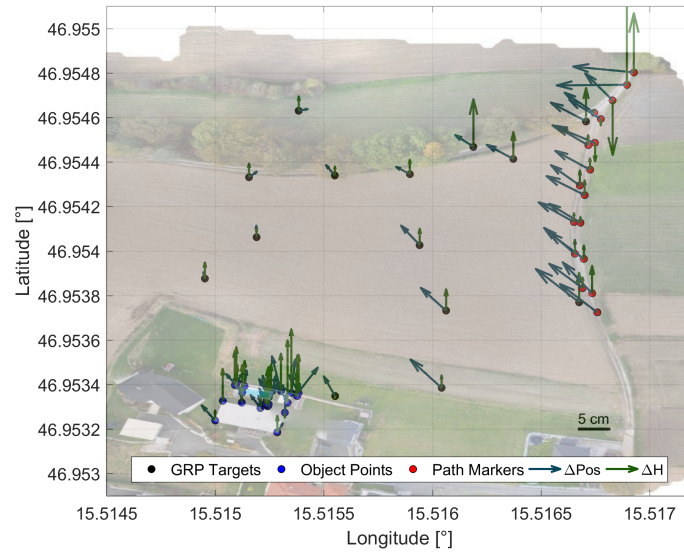
Errors from georeferencing are generally expected to result in global effects such as shift, rotation or scaling on all POI classes. Errors from the measurement of points in pictures can be different between the different POI classes (i.e. object points, GCPs and colour markers). As already mentioned in section 4.1.2, natural points (object points) tend to be much harder to identify in the pictures than GCPs or colour markers (see figure 4–2). The same is true for the measurement of those points by means of RTS. The placement of the reflector pole on a natural point (e.g. the corner of a wall, the centre of a manhole) cannot be done as exactly as on a GCP, which has a predefined notch to place the pole in. This leads to different point accuracies in different POI classes. Note however, that this difference in accuracy is not influenced by the georeferencing error, as this error effects all POI classes.

Figure 4–8 shows the difference of the photogrammetrically measured coordinates to the coordinates measured by RTS. The georeferencing was done conventionally, i.e. using GCPs.



**Figure 4–8:** Differences of POIs from conventional approach to RTS reference measurements.

GCP targets are depicted in black, object points are depicted in blue and colour markers along the path are depicted in red. The green arrows represent the height difference, while the blue arrows represent the position difference. The scale bar in the lower right corner refers to these differences. The differences of the GCP targets are smaller than the differences of the colour markers, which are themselves smaller than the differences of the object points. As described above, this is expected due to the different appearance of the POIs of each class. The mean 3d-difference of the GCPs amounts to 2.0 cm. In an actual measurement situation however it is more likely to measure natural points, rather than GCP targets. The object points are an example for such natural points. Their mean 3d-difference amounts to 6.6 cm. To compare these accuracies to the novel approach, figure 4–9 shows the differences of the coordinates from the novel georeferencing approach, i.e. using the GNSS positions of the pictures, to the RTS reference measurements.



**Figure 4–9:** Differences of POIs from novel approach to RTS reference measurements.

The mean 3d-difference of the object points amounts to 5.8 cm. This is similar to the object point difference using the conventional approach. However, if considering the GCPs and the colour markers only, an increase of the differences from west to east can be seen. This scaling factor becomes even more evident, when the photogrammetrically measured points from both approaches are compared to each other. Figure 4–10 shows the resulting differences.

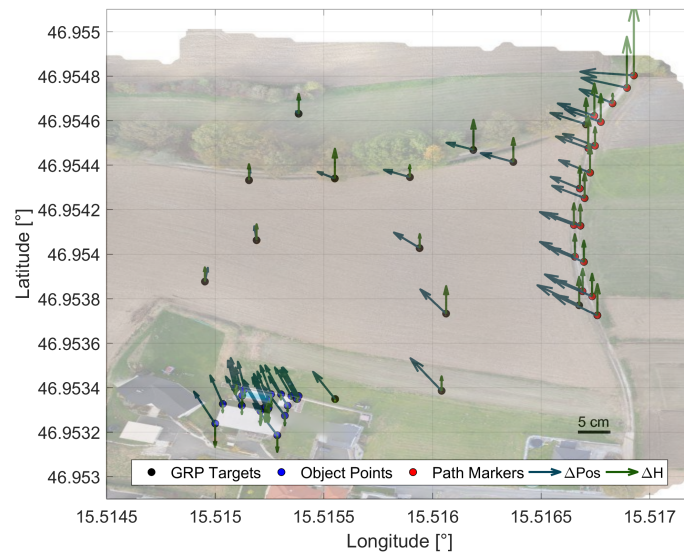


**Figure 4–10:** Differences of POIs from the novel approach to POIs from the conventional approach.

The scaling factor is more evident here, because the errors from the measurement of the points in the field using RTS can be completely eliminated. These errors mostly

influence the object points as described at the beginning of this section. Thus the here seen differences solely result from the different georeferencing approach. Note however that the absolute reference is lost, as two photogrammetric approaches are compared here. To gain a better understanding of this scale factor, the distances between POIs are compared to reference distances. The distances between the POIs are calculated from their coordinates, resulting from the different approaches. The reference distances are calculated from the local POI-coordinates measured by the RTS. Figure 4–11 shows the differences of the distances from the conventional and the novel approach to the reference distances from the RTS measurements.

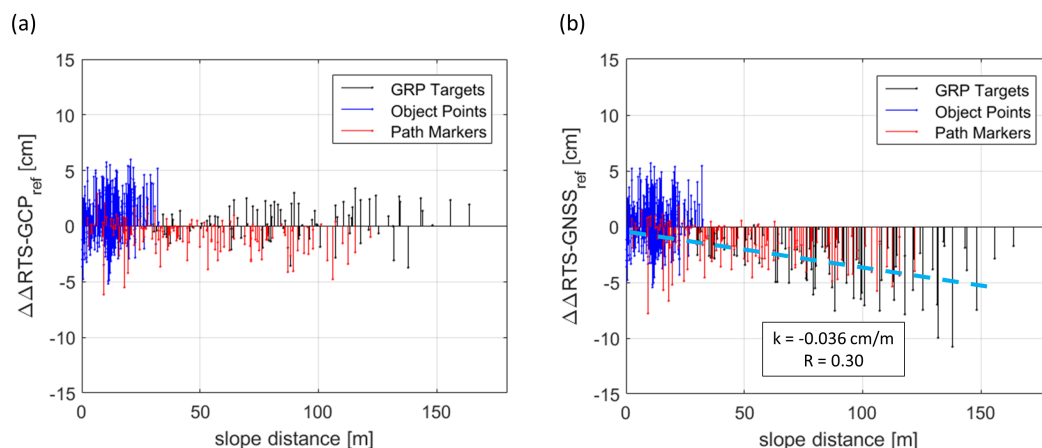


**Figure 4–11:** Differences of 3d distances between the POIs, to reference distances (from RTS measured coordinates): (a) POI coordinates from the conventional approach, and (b) POI coordinates from the novel approach.

The abscissa is the distance between the POIs, and the ordinate is the difference of this distance to the reference distance. Black stems indicate distances between GCPs, red stems indicate differences between colour markers, and blue stems indicate distances between object points. The distance differences for the object points are similar in both approaches with the mean absolute distance difference being 1.7 cm. Also, the pattern of these differences are similar in both figures. This suggests, that the differences are the result of the identification inaccuracy of those points both in the field and in the pictures.

The differences for GCPs and colour markers show different behaviour. In figure 4–11 (a), the differences do not seem to depend on the distance between the POIs, while in figure 4–11 (b), a clear trend is visible. This trend results in about 4 cm distance error between two points of 100 m distance between them. The origin of this trend remains unknown and would require further investigation.

### 4.2.3 Accuracy of deduced Values

In practice, a point cloud is rarely the final result of a photogrammetric survey. More often, values like volume, area or orientation are deduced from a subset of points of the point cloud. The Institute of Applied Geosciences at Graz University of Technology for example mostly determines the orientation of planar areas in rock faces. These planar

areas are the result of single rocks that broke out of the rock face. Together with other parameters such as material, roughness or moisture, the orientation of these planar areas can give information about the stability of the rock face. Hence this allows for an estimation of the risk of rocks breaking out of the rock face and falling down. Further information on this topic is given by Dewez 2016 [7].

The flight area at hand (section 4.1.1) does not contain any rock faces where the accuracy of deduced orientations could be assessed. Instead of that, the orientation of some rooftops of the buildings within the field of view of the camera were calculated and compared between the different approaches. Figure 4–12 shows the used rooftops as well as their labels (01-12).



**Figure 4–12:** Rooftops used for investigation of orientation accuracy. For rooftops 11 and 12, not only photogrammetric measurements from both approaches, but also RTS measurements are available.

The orientation of the rooftops was calculated by manually selecting the points within the area of interest (i.e. the current rooftop), and fitting a plane through these points. The normal vector of the plane defines its orientation in space. The orientation was calculated for all 12 rooftops, once from the DPC of the conventional approach and once from the DPC of the novel approach. The difference in angle and in perpendicular between the corresponding normal vectors (i.e. the orientations) of the rooftops 1-12 is depicted in figure 4–13.

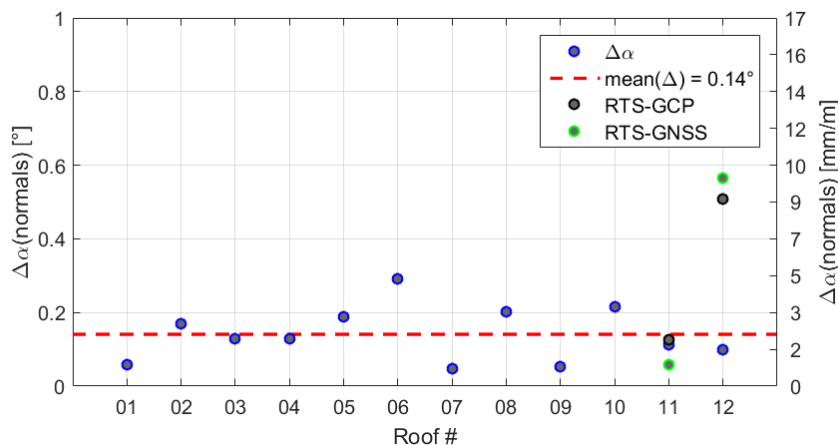


**Figure 4–13:** Difference between the normal vectors of the two approaches (blue) and absolute difference to RTS measurements (only available for 11 and 12).

The abscissa are the rooftop labels as presented in figure 4–12. The left ordinate is the difference between the normal vectors of corresponding roofs in degrees, and the right ordinate is the same difference in millimetres at a distance of 1 m from the rotation centre. The differences between the normal vectors of the GCP referenced- and the GNSS referenced data is shown in blue. For rooftops 11 and 12, also RTS measurements were taken allowing for an absolute reference. The difference to this actual reference is depicted in green and black, for GNSS referenced data and GCP referenced data respectively. For rooftop 12 i.e. the small shed (see figure 4–12), this difference to the reference is with about 0.5 degrees relatively large compared to the other rooftops. However this is still within the accuracy of 1-2 degrees for this application, as these orientations are conventionally measured manually by compass/clinometer [7]. For the larger rooftop (11), the difference between the photogrammetric approaches and the RTS reference measurements is around 0.1 degrees.

The mean difference between the orientations calculated from the different photogrammetric approaches amounts to 0.14 degrees, which corresponds to 2.4 mm per meter distance from the rotation centre. A Kolmogorow-Smirnow-Test showed that the differences between the two photogrammetric approaches are normally distributed with  $\mu = 0.14^\circ$  and  $\sigma = 0.07^\circ$  ( $\alpha = 5\%$ ).

## 5. Conclusion and Outlook

In the course of this thesis, a novel approach for direct georeferencing using relative GNSS solutions of photos taken from a UAS was assessed in terms of accuracy. The used AI-Botix X6 V2 hexacopter (section 2) contains a GNSS unit with a geodetic GNSS receiver and antenna. In section 3, the accuracy of the sensor position on the platform of the UAS was assessed under different GNSS conditions by total station reference measurements. Also the OTF GNSS solution that is calculated directly on board the UAS was compared to the PP GNSS solution that is calculated by a third party software (section 3.4). The coordinate transformation from the GNSS receiver position to the sensor position on the platform constitutes an essential part of the sensor accuracy. One of the inputs to the transformation function are the sensors offsets with respect to a reference point on the platform. Due to inconsistencies during the experiments, the reference point, as well as the direction of the sensor offsets and the precise time stamp of every event had to be reverse engineered (section 3.3.2). The accuracy of points measured from the UAS using the novel referencing approach was assessed in section 4. A comparison between corresponding point clouds from the conventional and the novel approach was carried out (section 4.2.1). Also, the coordinates of single points from 3 categories (i.e. object points, GCP targets and colour markers) were compared to reference coordinates measured by RTS (section 4.2.2). One application of the Institute of Applied Geosciences is the determination of rock face orientations. Therefore the orientation of building roofs was determined and compared to each other using both approaches (section 4.2.3).

The experiments concerning the sensor accuracy showed, that the OTF solution calculated on board the UAS shows a larger variance than the results from the PP solution. This occurs especially in the longitude component. The sensor accuracy when using the OTF solution was 10.2 cm. As no data except the solution is available for the user, the reason for this relatively low accuracy remains unknown. However for the purpose of positioning the drone during a flight, the real time accuracy is sufficient in most used cases. When calculating coordinates or a point cloud from the taken pictures though, the precise GNSS coordinates of the pictures should be calculated in post processing.

Using the PP solution, an accuracy of 2.2 cm in three flights on two different days could be reached under ideal GNSS conditions. Under problematic conditions (GNSS signals obstructed by a line of trees with leaves on them), this accuracy could not be reached. The leaves of the trees seemed to cause frequent loss and regain of single satellite signals, thus resulting in jumps of up to 20 cm in the coordinates. However the expected accuracy under ideal GNSS conditions could be regained almost instantly, once the UAS moved out of the obstructed space. When the leaves were fallen down from trees, we could not see a significant accuracy decrease to compared to ideal conditions. This however does not necessarily hold true for any obstruction by trees without leaves.

The point clouds calculated from the different approaches showed a mean difference of 2.9 cm. Around the edges of the point clouds, the difference increases to about 5-10 cm.

This can be the result of insufficient overlapping of the point clouds or blunders in one point cloud or the other. 95 % of the differences are below 6.5 cm. When comparing single POIs to RTS reference measurements, the accuracy of the object points was 6.6 cm for the conventional approach, and 5.8 cm for the novel approach. However when using the novel approach, a scale factor of 3.6 cm per 100 m occurred. The origin of this scale factor remains unknown and would require further investigation. Hence for now, the scale factor has to be considered when deducing values such as orientation or volume from the point cloud. As a rule of thumb, points that are more than 100 m apart from each other should not be used in the calculation of deduced values. The rock faces whose orientation is of interest for the Institute of Applied Geosciences are never larger than a few square meters, thus fulfilling the stated rule of thumb. The mean absolute difference between the orientation of rooftops from the conventional to the novel approach amounted to 0.14 degrees, which is sufficient for the used case of rock faces.

The accuracies found in this thesis were achieved using the reverse engineered sensor offsets for the transformation function of AIProFlight version 2.9.0.37. These sensor offsets do not coincide with the sensor offsets given by the company. As this is purely a software issue, the offsets can potentially be fixed with every update of AIProFlight. Therefore, the here found offsets only apply to this particular version of the software and would have to be verified for every new version of AIProFlight.

The global position of the sensor on the platform was calculated using relative GNSS measurements with a local base station. To increase efficiency of this approach even more, correction data from a network provider could be used. This data can be downloaded from a respective provider after the flight, since the novel approach requires post processing of the GNSS data anyway. Thus the UAS and its sensor (e.g. camera) would be the only required instruments in the field! The accuracy of the GNSS solution using network data is expected to be very similar to the accuracy when using a local base station, however this was not tested in the course of this thesis. Both EPOSA and APOS offer raw data from their stations which can be employed in relative GNSS post processing.

For geodetic applications the issue of efficiency in the field is clearly solved when using the novel approach, as we covered 30000 square meters in about 20 minutes. The post processing including the generation of a point cloud took about 1 hour in preparation and between 5 and 7 hours of computing time. The additional time that goes into extracting saleable information from the point cloud largely depends on the respective application. The scaling factor however prevents correct excavation volume calculation for large areas as often required in road, or tunnel construction. Façade survey would be a possible application for the approach, due to the smaller area to be covered. The legal restrictions have to be kept in mind though, as admittance from the officials has to be requested for every single flight within a city. These barriers still need to be overcome for the UAS technology to become standard equipment in geodetic and geotechnical applications.

# References

- [1] Bundesministerium für Verkehr, Innovation und Technologie. Website of the Federal Ministry for Traffic, Innovation and Technology. <https://www.bmvit.gv.at/verkehr/luftfahrt/drohnen> (visited in January 2018).
- [2] AIBotix. Aibot X6 V2 User Manual, Version 5.4, AIBotix GmbH, Kassel, Germany. 71 pages. 2016.
- [3] AIBotix. AiProFlight User Manual, Version 2.9, AIBotix GmbH, Kassel, Germany. 49 pages. 2016.
- [4] Suga Akira et al. Exchangeable image file format for digital still cameras: Exif Version 2.31. 186 pages. 2016.
- [5] Austro Control GmbH. Website of the Austrian Aeronautical Authority. <https://www.austrocontrol.at/drohnen> (visited in November 2017).
- [6] Rod Deakin. A Note on the Bursa-Wolf and Molodensky-Badekas Transformations. School of Mathematical and Geospatial Sciences, RMIT University. 21 pages. 2006.
- [7] T. J.B. Dewez et al. Facets : A cloudcompare plugin to extract geological planes from unstructured 3d point clouds. *International Archives of the Photogrammetry, Remote Sensing and Spatial Information Sciences - ISPRS Archives*, 41:799–804, 2016.
- [8] Eposa. Bedingungen über die Nutzung von EPOSA, Energie Burgenland AG, ÖBB-Infrastruktur AG, Wiener Netze GmbH, Vienna, Austria. 5 pages. 2015.
- [9] Daniel Girardeau-Montaut. CloudCompare version 2.6.1. user manual. 180 pages. 2015.
- [10] Zan Gojcic. Synchronization routine for real-time synchronization of modern total stations. 90 pages. *Master Thesis*, 2016.
- [11] Christoph Holst, Berit Schmitz, Schraven Achim, and Heiner Kuhlmann. Eignen sich in Standardsoftware implementierte Punktwolkenvergleiche zur flächenhaften Deformationsanalyse von Bauwerken. *zfv*, (2):98 – 110, 2017.
- [12] J. J. Hutton et al. Centimeter-Level, Robust Gns-Aided Inertial Post-Processing for Mobile Mapping Without Local Reference Stations. *ISPRS - International Archives of the Photogrammetry, Remote Sensing and Spatial Information Sciences*, (1):819 – 826, 2016.
- [13] D Lague, N Brodu, and J Leroux. Accurate 3D comparison of complex topography with terrestrial laser scanner: Application to the Rangitikei canyon (NZ). *ISPRS Journal of Photogrammetry and Remote Sensing*, (82):10 – 26, 2013.
- [14] Werner Lienhart, Matthias Ehrhart, and Magdalena Grick. High frequent total station measurements for the monitoring of bridge vibrations. *Journal of Applied Geodesy*, 11(1):1–8, 2016.

## 5. REFERENCES

---

- [15] Thomas Luhmann, Stuard Robson, Stephen Kyle, and Ian Harley. Close Range Photogrammetry. 510 pages. 2011.
- [16] Wolfgang Niemeier. Ausgleichsrechnung - Statistische Auswertemethoden. 493 pages. 2008.
- [17] NovAtel. A NovAtel Precise Positioning Product Inertial Explorer ® User Guide, NovAtel Inc., Calgary, Canada. 194 pages. 2013.
- [18] Novatel. Datasheet of the GPS-703-GGG-HV Antenna, NovAtel Inc., Calgary, Canada. 2 pages. 2015.
- [19] Lothar Sachs. Angewandte Statistik - Anwendung statistischer Methoden. 889 pages. 2002.
- [20] Travis Wiens and Stuart Bradley. A Comparison of Time Delay Estimation Methods for Periodic Signals. [http://www.nutaksas.com/papers/wiens\\_dsp\\_delay.pdf](http://www.nutaksas.com/papers/wiens_dsp_delay.pdf) (visited in November 2016). 2009.

# A. Results of experiments under ideal GNSS conditions

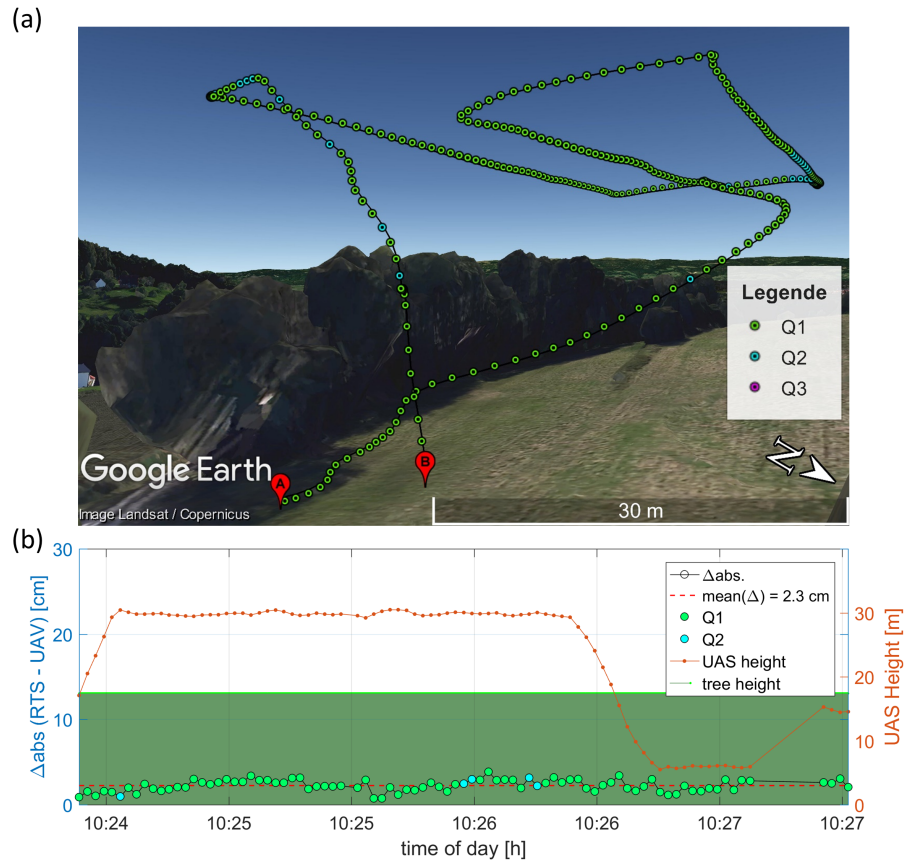


**Figure A-1:** Flight Nr. 0005, 16.03.2017: Ideal GNSS conditions, PP-approach: a) quality of the GNSS solution (see table 3-3), and b) difference to the reference trajectory with obstacle height (trees), flight height of the UAS and GNSS quality of the used point.

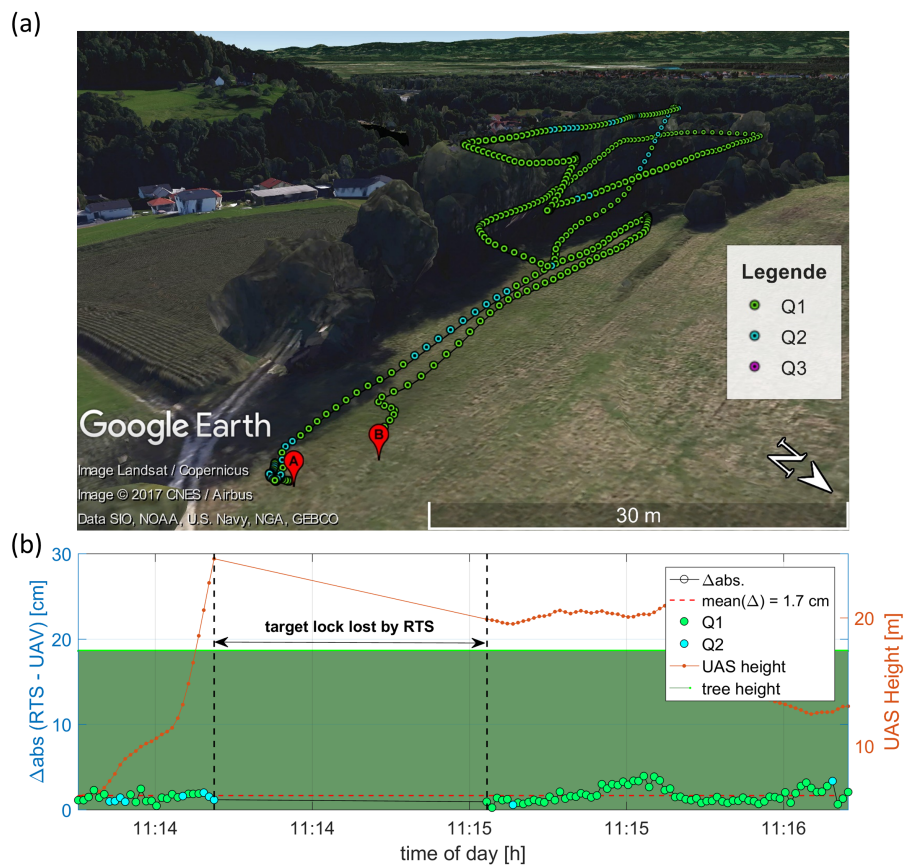


**Figure A-2:** Flight Nr. 0007, 16.03.2017: Ideal GNSS conditions, PP-approach: a) quality of the GNSS solution (see table 3-3), and b) difference to the reference trajectory with obstacle height (trees), flight height of the UAS and GNSS quality of the used point.

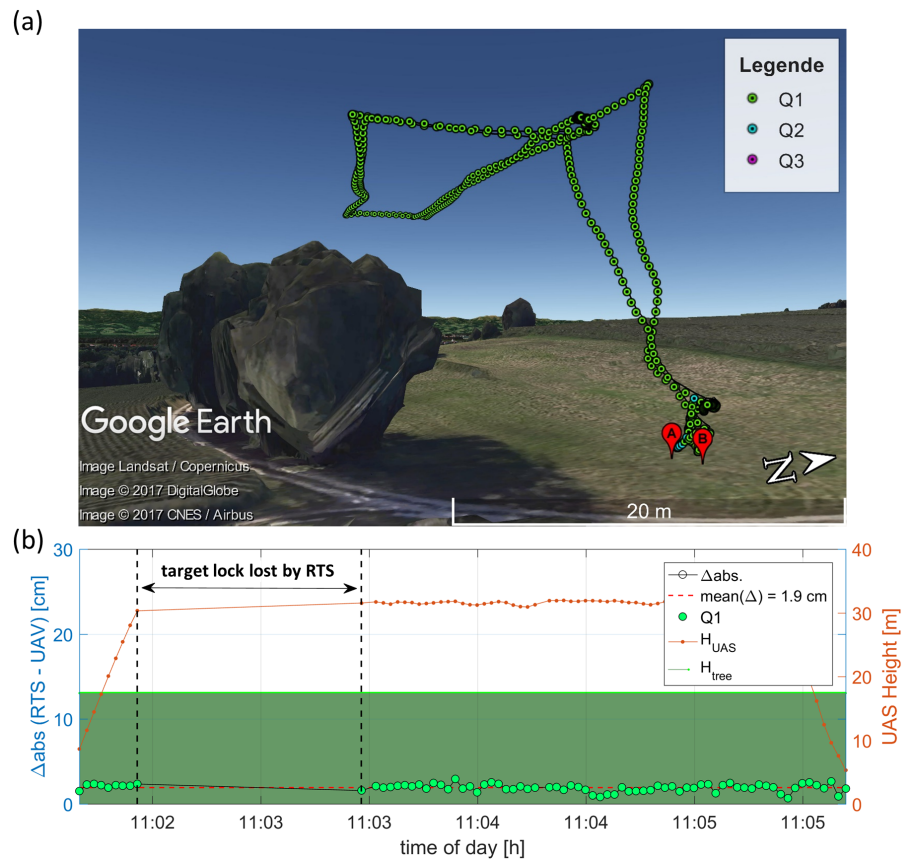
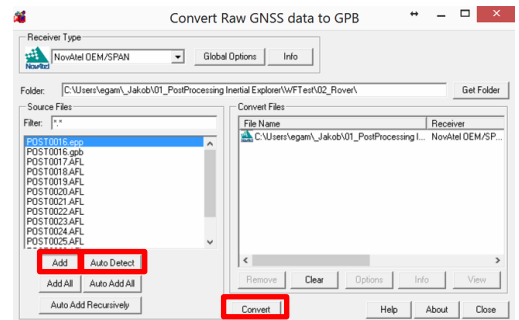


**Figure A-3:** Flight Nr. 0020, 20.07.2017: Ideal GNSS conditions, PP-approach: a) quality of the GNSS solution (see table 3-3), and b) difference to the reference trajectory with obstacle height (trees), flight height of the UAS and GNSS quality of the used point.

## **B. Workflow in Inertial Explorer**

1. Create a Project:
  - a. File → New Project → Empty Project
2. Convert the .AFL raw data file from the UAS and the RINEX raw data file from the base station to the Inertial Explorer GPB format:

- a. File → Convert → Raw GNSS to GPB
- b. click **Auto Detect** and **add** all files you want to convert from the source files (left) to the convert files (right) and press **convert**



3. Make sure that the observations of the UAS are specified as **kinematic** and the observations of the Base station are specified as **static**

- a. File → GPB Utilities → View Raw GNSS Data → select the respective GPB file
- b. Under **Mode** it should say **Kinematic** for the rover (i.e. the drone) file, and **Static** for the base station file. If it is in wrong mode, go to **Edit → Switch Static/Kinematic** → select the wanted process mode (static for base, kinematic for UAS), make sure **All Epochs** is selected and start Location **From Start** is selected and click **OK**.

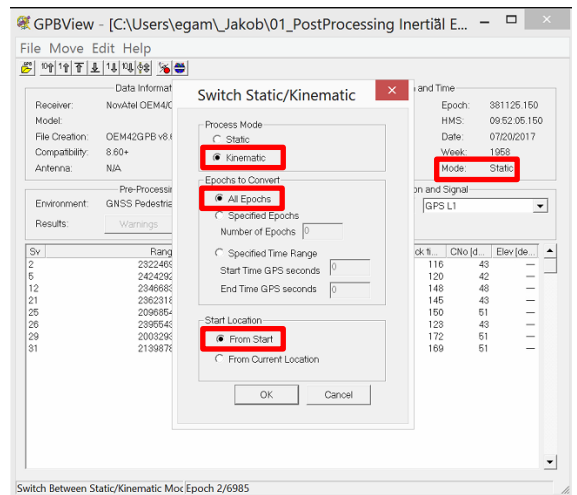
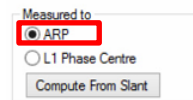
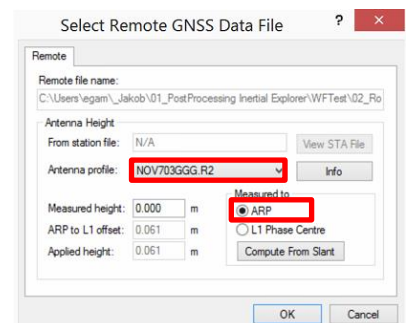


Figure 1: Switching the processing mode from static to kinematic

4. Load the Rover and the Base station file:
  - a. File → Add Master File(s) → select the Base Station GPB file
    - i. make sure the Phase Centre Offset is measured to the Absolute Reference Point (**ARP**) The Antenna profile will be detected automatically from the RINEX file.



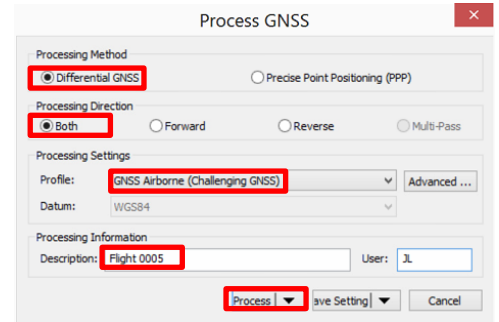
- b. File → Add Remote File → select the UAS GPB file
  - i. select the Antenna profile **NOV703GGG.R2** and check measured to **ARP**



5. Process the data

a. Process → Process GNSS

- i. select **Differential GNSS**
- ii. select **Both** Processing Directions
- iii. Select **GNSS AIRBorne (Challenging GNSS)**
- iv. Press **Process** → Inertial explorer will now tell you that the sample frequency of master and remote file is different. Check “try to fix issues before processing”, and press *continue*.



6. Export the data:

a. Output → Export Wizard

- i. Select a file you want to export to by clicking **Browse** (Attention, if you forget that, the last exported file gets overwritten)
- ii. Select the **AIProFlight** Profile (this exists only on Georgs PC)
- iii. press **next** 4 times (check the default values, they should be self explanatory) and then press **finish**



The here created file can be imported to AIProFlight as Post Processing Coordinates (see AIProFlight User Manual page 42).

## C. Processing Reports from Agisoft PS

### C.1 Processing Report from Agisoft PS using the conventional approach

# GCPs-Model-optimized

APS automatically generated report  
07 November 2017



# Survey Data

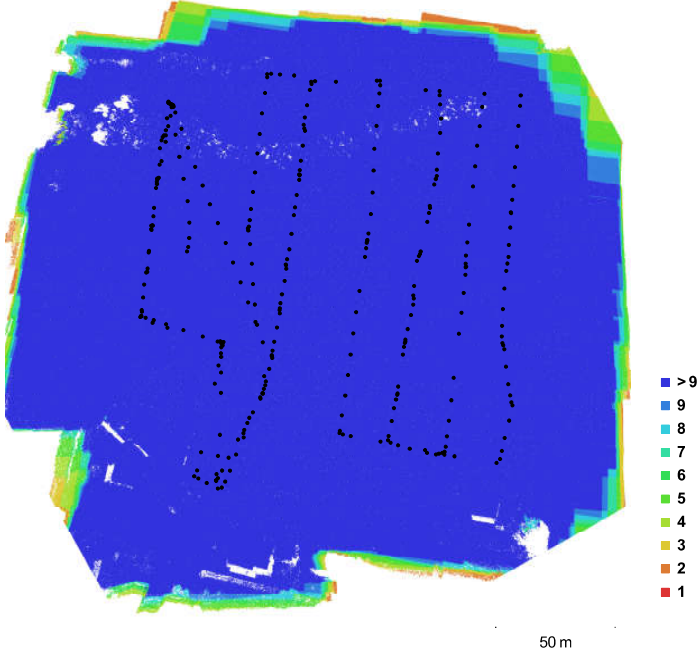


Fig. 1. Camera locations and image overlap.

Number of images:	317	Camera stations:	316
Flying altitude:	68.9 m	Tie points:	8,217
Ground resolution:	1.9 cm/pix	Projections:	108,815
Coverage area:	0.0562 km <sup>2</sup>	Reprojection error:	0.632 pix

Camera Model	Resolution	Focal Length	Pixel Size	Precalibrated
E-PL5	(12 mm) 4608 x 3456	12 mm	3.75 x 3.76 μm	Yes

Table 1. Cameras.

## Camera Calibration

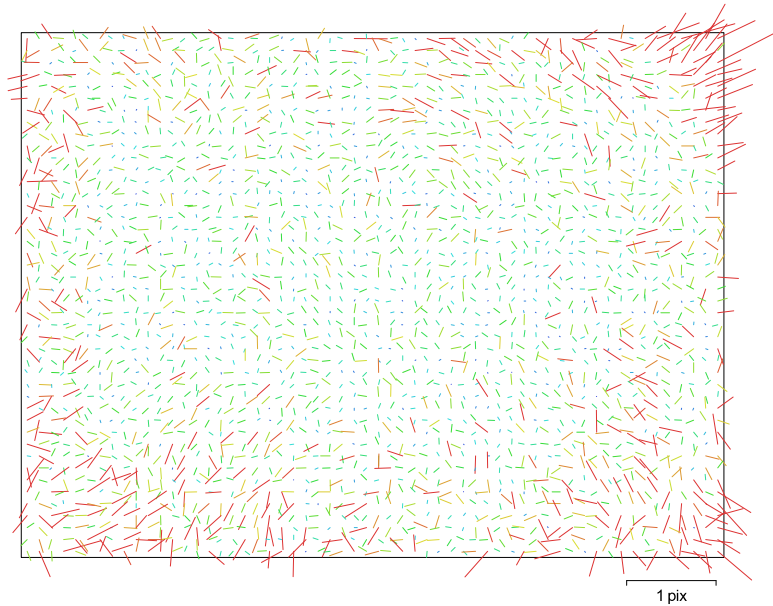


Fig. 2. Image residuals for E-PL5 (12 mm).

**E-PL5 (12 mm)**  
317 images

Resolution	Focal Length	Pixel Size	Precalibrated
4608 x 3456	12 mm	3.75 x 3.76 $\mu\text{m}$	Yes
Type:	Frame	F:	3259.91
Cx:	-54.8909	B1:	-1.76479
Cy:	-9.7874	B2:	0.8847
K1:	-0.020778	P1:	-0.00185229
K2:	0.00129613	P2:	0.000426995
K3:	0.0094221	P3:	0
K4:	-0.00716482	P4:	0

## Ground Control Points



Fig. 3. GCP locations.

Count	X error (cm)	Y error (cm)	Z error (cm)	XY error (cm)	Total (cm)	Image (pix)
4	1.11475	1.14396	0.708737	1.59728	1.74746	0.199

Table 2. Control points RMSE.

Count	X error (cm)	Y error (cm)	Z error (cm)	XY error (cm)	Total (cm)	Image (pix)
57	1.93294	2.47778	4.62945	3.14255	5.5953	0.507

Table 3. Check points RMSE.

Label	X error (cm)	Y error (cm)	Z error (cm)	Total (cm)	Image (pix)
08	-0.0553641	-1.59289	-1.08731	1.92941	0.188 (9)
09	-1.78427	0.161005	0.808066	1.96532	0.099 (32)
01	0.680357	1.62314	-0.289542	1.78362	0.249 (73)
15	1.14939	-0.19179	0.300305	1.20336	0.108 (23)
<b>Total</b>	<b>1.11475</b>	<b>1.14396</b>	<b>0.708737</b>	<b>1.74746</b>	<b>0.199</b>

Table 4. Control points.

Label	X error (cm)	Y error (cm)	Z error (cm)	Total (cm)	Image (pix)
02	-0.298449	0.530958	1.17104	1.31997	0.241 (71)
03	-1.0465	1.05649	0.370965	1.53263	0.276 (58)
04	-1.30329	-0.834293	3.10806	3.47198	0.271 (11)
05	-1.87452	0.0202826	-0.349887	1.907	0.308 (33)
06	-1.33041	-1.02947	-2.65285	3.14125	0.240 (26)
07	-0.914694	-1.18018	-0.412038	1.54895	0.182 (35)
10	0.260354	-2.92718	-0.155238	2.94284	0.196 (46)
11	0.0131848	0.936392	0.337487	0.99544	0.166 (48)
12	-1.65491	1.67699	-0.202654	2.36476	0.215 (64)
13	-0.0856723	0.317952	0.933978	0.990328	0.294 (59)
14	-1.09975	-0.863299	-0.346851	1.4405	0.305 (63)
P01	-3.1464	-1.09911	-9.94154	10.4853	0.769 (18)
P02	-1.04403	-1.35441	-6.42245	6.64623	0.948 (19)
P03	-1.64107	3.0911	-10.2471	10.8283	1.075 (14)
P04	-3.69749	2.55393	-0.696342	4.54741	0.671 (11)
P05	-4.51081	4.92906	-4.94915	8.31487	0.820 (11)
P06	-1.18881	3.67333	-4.97986	6.30124	0.429 (7)
P07	-1.67989	6.56383	-6.10871	9.12262	0.782 (8)
P08	-2.2018	3.15799	-3.92261	5.49615	0.606 (7)
P09	-2.2594	4.11195	-3.81949	6.04992	1.187 (8)
P10	-1.16232	3.52683	-1.8683	4.15693	0.677 (8)
P11	-4.0843	2.57356	-5.36494	7.21715	0.842 (9)
P12	-3.69592	2.94401	-4.15995	6.29541	0.782 (9)

Label	X error (cm)	Y error (cm)	Z error (cm)	Total (cm)	Image (pix)
P13	-3.30261	-0.140655	-5.5579	6.46663	0.731 (9)
P14	-3.45943	1.66694	-7.12583	8.09467	0.670 (8)
P17	-0.754786	2.65	-3.04564	4.10708	0.437 (8)
P18	-1.09248	0.205841	-5.65239	5.76067	0.705 (9)
P19	-2.05777	2.32895	-4.74268	5.67023	0.523 (9)
P21	-0.290602	2.30126	-6.71815	7.10731	0.557 (16)
P22	-1.05093	1.79479	-5.84416	6.20322	0.775 (17)
P23	-1.3637	2.59467	-5.00349	5.79887	0.682 (15)
P24	-0.0290565	4.64769	-5.47107	7.17875	0.803 (15)
P25	0.372758	3.54161	-3.90109	5.28209	0.553 (15)
P26	-0.893785	1.80093	-3.35877	3.91452	0.466 (14)
P28	-5.53117	0.608868	-6.01668	8.19543	0.613 (18)
P29	-3.03632	3.6467	-3.73832	6.04092	1.039 (16)
P30	0.669802	3.55662	-4.53684	5.80354	1.034 (17)
P31	-0.984299	2.33641	-5.97736	6.4928	0.749 (18)
P33	-1.01576	2.29811	-6.20299	6.69255	0.689 (13)
P34	-2.29084	3.39834	-6.00898	7.27354	0.781 (15)
W01	-0.658534	-1.66252	1.76176	2.51027	0.355 (12)
W02	-0.638417	-2.40568	1.29764	2.80691	0.279 (12)
W03	0.208082	-1.46831	1.95989	2.45773	0.265 (11)
W04	-0.042383	-1.87369	1.08879	2.16748	0.320 (10)
W05	-0.051262	-1.50408	3.31258	3.63842	0.229 (8)
W06	-1.04749	-1.70894	4.36228	4.80075	0.460 (4)
W07	1.09703	-0.461972	2.28204	2.57383	0.062 (2)
W08	3.79868	2.29733	-8.36976	9.47421	0.011 (2)
W09	-0.858189	-2.81684	9.62068	10.0612	0.307 (3)
W10	-0.642069	-1.40088	5.15544	5.38083	0.228 (4)
W11	1.59153	-1.18693	5.57329	5.91636	0.216 (5)
W13	0.573298	-1.36497	2.43114	2.84645	0.200 (8)
W14	0.868411	-1.45303	1.53863	2.28754	0.278 (9)
W15	-0.462053	-1.34296	2.32552	2.7249	0.323 (11)
W16	-0.0255954	-2.64355	1.19602	2.90163	0.231 (12)
W17	-1.48974	-3.09819	-0.736247	3.5157	0.362 (12)

Label	X error (cm)	Y error (cm)	Z error (cm)	Total (cm)	Image (pix)
W18	-1.08121	-1.61167	4.69681	5.08198	0.303 (12)
<b>Total</b>	<b>1.93294</b>	<b>2.47778</b>	<b>4.62945</b>	<b>5.5953</b>	<b>0.507</b>

Table 5. Check points.

## Digital Elevation Model

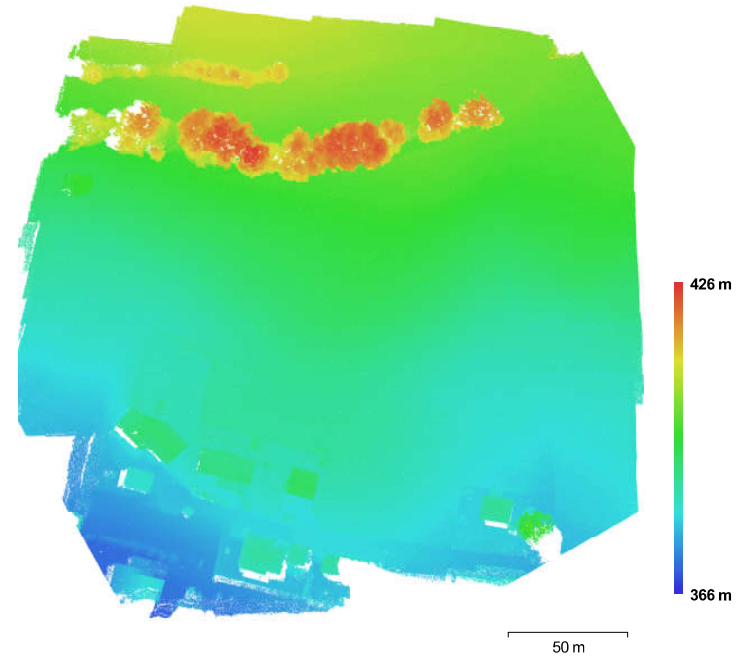


Fig. 4. Reconstructed digital elevation model.

Resolution: unknown  
Point density: unknown

# Processing Parameters

## General

Cameras	317
Aligned cameras	316
Markers	61
Coordinate system	WGS 84 (EPSG:4326)

## Point Cloud

Points	8,217 of 10,384
RMS reprojection error	0.257124 (0.631976 pix)
Max reprojection error	1.90065 (9.98444 pix)
Mean key point size	2.42676 pix
Effective overlap	15.3085

## Alignment parameters

Accuracy	High
Pair preselection	Generic
Key point limit	4,000
Tie point limit	400
Constrain features by mask	No
Adaptive camera model fitting	Yes
Matching time	17 minutes 34 seconds
Alignment time	41 seconds

## Optimization parameters

Parameters	f, b1, b2, cx, cy, k1-k4, p1, p2
Optimization time	3 seconds

## Depth Maps

Count	315
-------	-----

## Reconstruction parameters

Quality	Medium
Filtering mode	Mid
Processing time	2 hours 44 minutes

## Dense Point Cloud

Points	13,198,219
--------	------------

## Reconstruction parameters

Quality	Medium
Depth filtering	Mid
Depth maps generation time	2 hours 44 minutes
Dense cloud generation time	34 minutes 11 seconds

## Software

Version	1.2.6 build 2834
Platform	Windows 64 bit

## **C.2 Processing Report from Agisoft PS using the novel approach**

## GNSS+Scale-Model

APS automatically generated report  
30 November 2017



## Survey Data

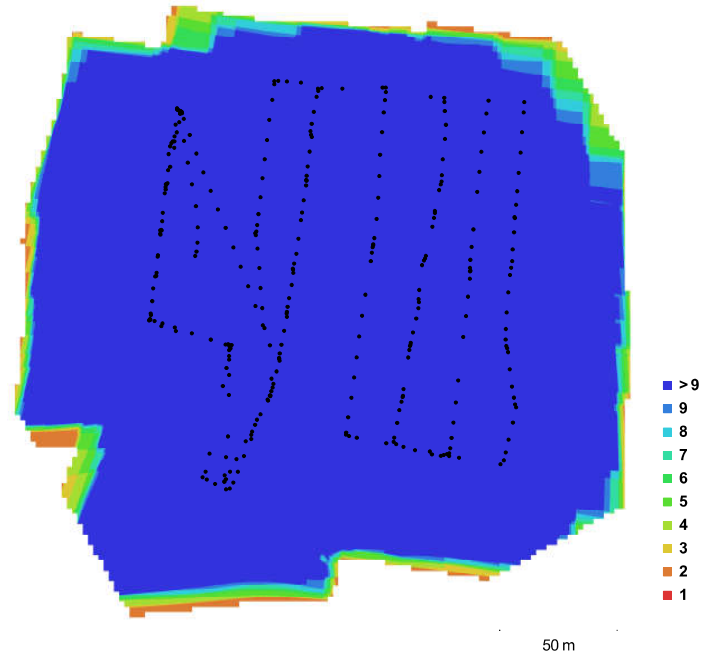


Fig. 1. Camera locations and image overlap.

Number of images:	317	Camera stations:	316
Flying altitude:	68.9 m	Tie points:	8,315
Ground resolution:	1.9 cm/pix	Projections:	114,642
Coverage area:	0.0572 km <sup>2</sup>	Reprojection error:	0.542 pix

Camera Model	Resolution	Focal Length	Pixel Size	Precalibrated	
E-PL5	(12 mm)	4608 x 3456	12 mm	3.75 x 3.76 $\mu$ m	Yes

Table 1. Cameras.

## Camera Calibration

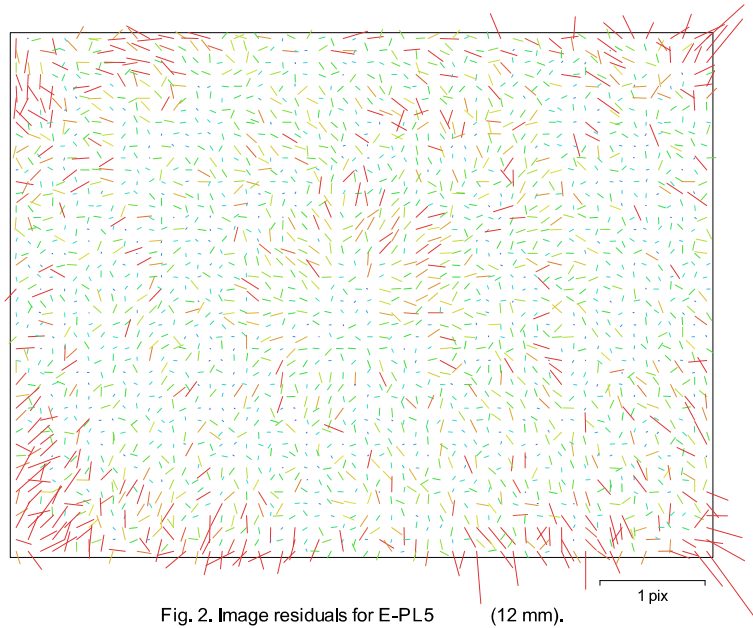


Fig. 2. Image residuals for E-PL5 (12 mm).

**E-PL5** (12 mm)  
317 images

Resolution	Focal Length	Pixel Size	Precalibrated
<b>4608 x 3456</b>	<b>12 mm</b>	<b>3,75 x 3,76 <math>\mu</math>m</b>	<b>Yes</b>
Type:	Frame	F:	3261.26
Cx:	-61.4089	B1:	-1.66362
Cy:	-12.5101	B2:	-0.517371
K1:	-0.0254505	P1:	-0.00194272
K2:	0.0260489	P2:	0.000340115
K3:	-0.0368484	P3:	0
K4:	0.0209431	P4:	0

## Camera Locations

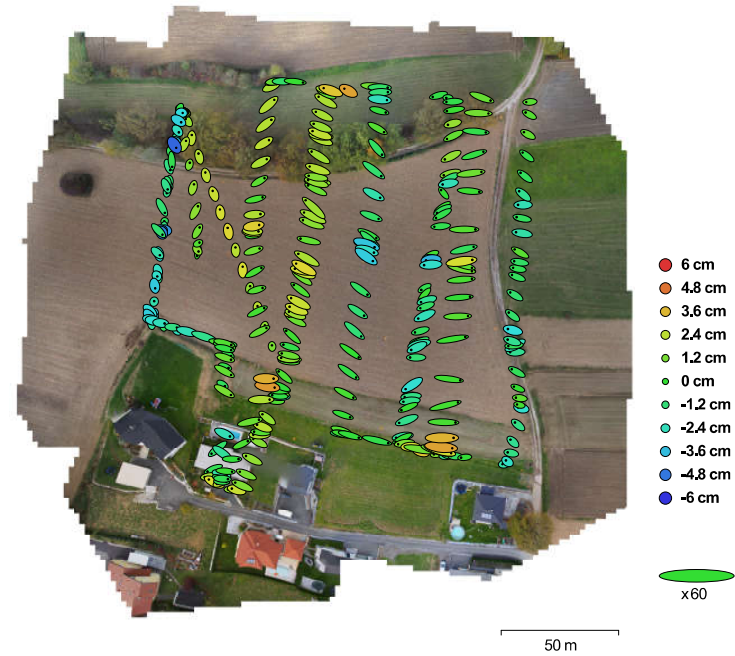


Fig. 3. Camera locations and error estimates.  
Z error is represented by ellipse color, X,Y errors are represented by ellipse shape.  
Estimated camera locations are marked with a black dot.

X error (cm)	Y error (cm)	Z error (cm)	XY error (cm)	Total error (cm)
8,52037	3,52869	1,77623	9,22217	9,39167

Table 2. Average camera location error.

# Ground Control Points



Fig. 4. GCP locations.

Count	X error (cm)	Y error (cm)	Z error (cm)	XY error (cm)	Total (cm)	Image (pix)
61	3,85339	4,3727	4,40096	5,82831	7,30326	0,713

Table 3. Check points RMSE.

Label	X error (cm)	Y error (cm)	Z error (cm)	Total (cm)	Image (pix)
02	0.0509123	-2.50786	-1.21097	2.78539	0.490 (71)
03	-1.20679	-1.20055	-2.02229	2.64335	0.497 (58)
04	1.36344	-2.30614	-1.35983	3.00439	0.645 (11)
05	2.10237	-1.58053	-2.13756	3.38928	0.875 (33)
06	2.83171	-2.56443	-7.14429	8.10159	0.590 (26)
07	4.1046	-3.1155	-4.01553	6.53288	0.366 (35)
08	5.44793	-4.09039	-4.9766	8.43669	0.226 (9)
09	-1.3685	-0.401781	-2.16478	2.59239	0.477 (32)
10	6.6768	-7.28928	-4.41186	10.8249	0.372 (46)
11	4.79592	-6.223	-1.85252	8.07207	0.450 (48)
12	1.74795	-4.33315	0.193653	4.67643	0.682 (64)
13	3.88844	-5.02137	-3.21251	7.11718	0.418 (59)
14	2.87466	-4.27223	-2.43713	5.69695	0.688 (63)
01	0.224081	-1.41058	-2.42851	2.81738	0.414 (73)
P01	-0.60897	-7.37973	-9.55628	12.0894	0.842 (18)
P02	1.37505	-7.65372	-5.60183	9.58388	1.195 (19)
P03	1.26976	-3.27422	-9.33559	9.97427	1.176 (14)
P04	-0.222498	-4.04081	0.76547	4.11869	0.888 (11)
P05	-0.822457	-2.01694	-2.48201	3.30225	1.300 (11)
P06	2.06368	-3.35974	-1.52958	4.22921	0.408 (7)
P07	0.231312	0.336348	-4.83165	4.84886	0.934 (8)
P08	0.282561	-3.21509	-2.65184	4.17719	0.709 (7)
P09	0.407108	-2.24023	-1.7945	2.89907	1.375 (8)
P10	1.52073	-2.85121	0.253707	3.24136	0.637 (8)
P11	-2.10961	-3.83539	-3.32852	5.49906	0.951 (9)
P12	-1.71305	-3.49916	-1.91638	4.34179	1.004 (9)
P13	-1.288	-6.5964	-3.34288	7.50642	0.749 (9)
P14	-1.33219	-4.75681	-5.52867	7.41405	0.758 (8)
P17	1.38549	-3.77221	-1.46949	4.27885	0.474 (8)
P18	0.925421	-6.24837	-3.45634	7.20033	0.615 (9)
P19	-0.0690653	-4.11376	-2.52516	4.82744	0.511 (9)
P21	1.4356	-4.03336	-4.57515	6.26586	1.124 (16)

Label	X error (cm)	Y error (cm)	Z error (cm)	Total (cm)	Image (pix)
P22	0.593548	-4.44158	-3.98275	5.99518	1,153 (17)
P23	-0.317681	-3.4348	-3.78177	5,11865	1,010 (15)
P24	1.01005	-1.50293	-4,15028	4,52812	1,399 (15)
P25	1.47258	-2.47659	-2.99165	4,15355	0,833 (15)
P26	0.111503	-4.05942	-2.38055	4,70726	0,842 (14)
P28	-3.14069	-5.67588	-5,71608	8,64599	0,907 (18)
P29	-0.542947	-2.65053	-3,34899	4,30533	1,322 (16)
P30	3.17309	-2.74481	-4,15678	5,90604	1,034 (17)
P31	1.42285	-3.93919	-5,70188	7,07483	0,963 (18)
P33	-0.150505	-3.41642	-5,0635	6,11012	1,033 (13)
P34	-1.22366	-2.6066	-5,13269	5,88525	1,330 (15)
W01	5.15191	-5.33073	-1,58941	7,58189	0,440 (12)
W02	4.72897	-5.66376	-2,07539	7,66477	0,373 (12)
W03	5.44664	-4.31157	-1,3035	7,06786	0,430 (11)
W04	4.4645	-4.50603	-2,2624	6,73458	0,565 (10)
W05	4.91738	-4.10531	-1,52671	6,58521	0,436 (8)
W06	4.58372	-4.41674	-0,486855	6,38397	0,567 (4)
W07	9.33092	-1.2606	-8,86023	12,929	0,075 (2)
W08	10.7964	0.149746	-16,0144	19,3144	0,096 (2)
W09	4.24142	-5.90929	8,18235	10,9481	0,442 (3)
W10	4.86091	-4.19784	0,972506	6,49585	0,225 (4)
W11	6.53852	-3.83318	2,76163	8,06673	0,293 (5)
W13	5.3411	-4.15454	-1,67235	6,97025	0,325 (8)
W14	5.87412	-4.16832	-2,19764	7,53059	0,504 (9)
W15	4.80906	-4.16138	-0,855896	6,4169	0,466 (11)
W16	5.42505	-5.85867	-2,01289	8,23449	0,355 (12)
W17	4.53	-6.83059	-4,13677	9,181	0,370 (12)
W18	5.75134	-6.24543	-0,0164936	8,49021	0,478 (12)
15	9.59694	-9.44714	-3,65817	13,9546	0,299 (23)
<b>Total</b>	<b>3,85339</b>	<b>4,3727</b>	<b>4,40096</b>	<b>7,30326</b>	<b>0,713</b>

Table 4. Check points.

## Scale Bars

Label	Distance (m)	Error (m)
PA250420.JPG_PA250470.JPG	159.475	-0,000914551
PA250470.JPG_PA250592.JPG	128.491	0,0630231
PA250592.JPG_PA250623.JPG	154.669	-0,0185573
PA250420.JPG_PA250623.JPG	147.871	-0,0408491
PA250420.JPG_PA250592.JPG	206.061	-0,0147327
PA250470.JPG_PA250623.JPG	211.813	0,0188627
<b>Total</b>		<b>0,0330621</b>

Table 5. Control scale bars.

## Digital Elevation Model

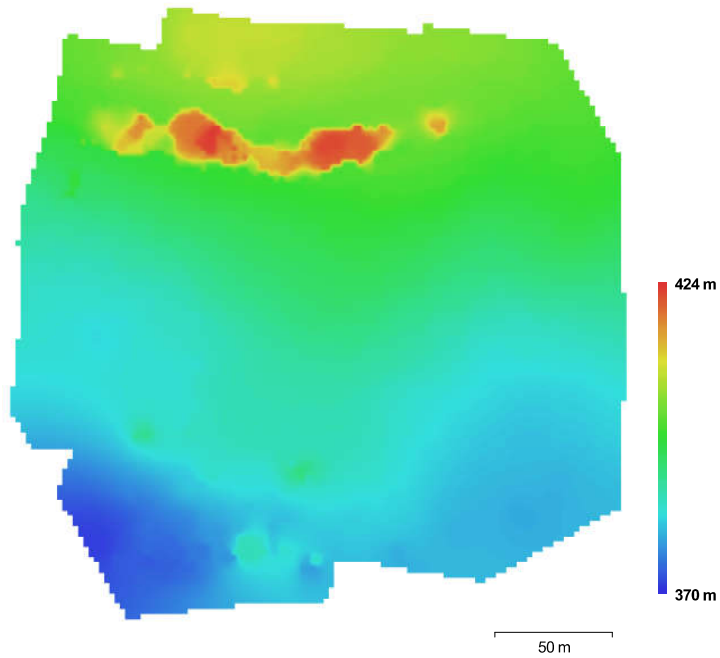


Fig. 5. Reconstructed digital elevation model.

Resolution: 2.22 m/pix  
 Point density: 0.204 points/m<sup>2</sup>

## Processing Parameters

<b>General</b>	
Cameras	317
Aligned cameras	316
Markers	61
Scale bars	6
Coordinate system	WGS 84 (EPSG:4326)
<b>Point Cloud</b>	
Points	8,315 of 10,433
RMS reprojection error	0.212339 (0.541969 pix)
Max reprojection error	0.642368 (22.3085 pix)
Mean keypoint size	2.43825 pix
Effective overlap	15.5673
<b>Alignment parameters</b>	
Accuracy	High
Pair preselection	Reference
Keypoint limit	4,000
Tie point limit	400
Constrain features by mask	No
Adaptive camera model fitting	Yes
Matching time	9 minutes 39 seconds
Alignment time	42 seconds
<b>Depth Maps</b>	
Count	315
<b>Reconstruction parameters</b>	
Quality	Medium
Filtering mode	Mld
Processing time	2 hours 42 minutes
<b>Dense Point Cloud</b>	
Points	12,768,500
<b>Reconstruction parameters</b>	
Quality	Medium
Depth filtering	Mld
Depth maps generation time	2 hours 42 minutes
Dense cloud generation time	33 minutes 39 seconds
<b>DEM</b>	
Size	178 x 183
Coordinate system	WGS 84 (EPSG:4326)
<b>Reconstruction parameters</b>	
Source data	Sparse cloud
Interpolation	Enabled
Processing time	0 seconds
<b>Orthomosaic</b>	
Size	13,994 x 13,877
Coordinate system	WGS 84 (EPSG:4326)
Channels	3, uint8
Blending mode	Nbsaic
<b>Reconstruction parameters</b>	
Surface	DEM
Enable color correction	No
Processing time	7 minutes 55 seconds
<b>Software</b>	
Version	1.2.6 build 2834
Platform	Windows 64 bit